

Reliability of Marine Structures Program

NONLINEAR RANDOM OCEAN WAVES: PREDICTION AND COMPARISON WITH DATA

Alok K. Jha

Supervised by
Steven R. Winterstein

Civil Engineering Department, Stanford University

20011123 058

DISTRIBUTION STATEMENT A
Approved for Public Release
Distribution Unlimited

June 1997
Report No. RMS-24



Department of CIVIL ENGINEERING
STANFORD UNIVERSITY

**NONLINEAR RANDOM OCEAN WAVES:
PREDICTION AND COMPARISON WITH DATA**

Alok K. Jha

Supervised by
Steven R. Winterstein

Civil Engineering Department, Stanford University

June 1997
Report No. RMS-24

Acknowledgements

This study is part of the doctoral work of the author and has been supported by the Office of Naval Research, grant N00014-95-1-0366, under the supervision of Dr. Peter Majumdar, and grant N00014-96-1-0641, under the supervision of Dr. Roshdy S. Barsoum. Additional funding has been provided by the Reliability of Marine Structures (RMS) program at Stanford University. The author thanks Dr. Sverre Haver of Statoil for providing the North Sea wave data and Dr. Tom Marthinsen of Saga Petroleum for providing the wave tank data.

Abstract

Second-order nonlinear models have been increasingly used in recent years to model nonlinear processes in offshore engineering. We develop convenient analytic formulae to predict the nonlinearities in waves and to predict the crest height distribution in a specified wave condition. We apply such models to study the properties of random ocean waves. These include measured waves both in wave tanks and in field. Statistics comparison between model and measurements include: moment comparisons, comparison of distributions of wave elevations, crest heights, wave heights, and conditional distributions of local wave parameters, for example, crest height given wave heights, wave periods given crest heights, among others.

We find the second-order model predictions to agree quite closely with the field measurements, while the wave tank statistics seem to be underpredicted by the second-order model.

Finally, we solve the inverse problem, in which we identify the underlying first-order wave components, which when run through the second-order wave predictor matches the measured wave histories time point by time point.

Contents

Acknowledgements	iii
Abstract	v
1 Prediction of Second-Order Waves	1
1.1 Introduction	1
1.2 Wave Model	2
1.3 Comparison of α_3 and α_4 : Data vs. Prediction Models	8
1.4 Distribution Comparisons	13
1.4.1 Summary of Measured Wave Data Sets	13
1.4.2 Summary of Simulated Wave Data	21
1.4.3 Comparison of Wave Elevation Distributions	22
1.4.4 Comparison of Crest Height Distributions	33
1.4.5 Comparison of Wave Height Distributions	41
1.5 Comparison of Local Wave Statistics	46
2 Identification of First-Order Waves	51
2.1 Methodology	52
2.2 Verification	57
2.2.1 Identification of components for simulated data	57
2.2.2 Identification of components for wave tank data	58
3 Conclusions and Recommendations	63

Bibliography

66

List of Tables

1.1	Summary information of the four wave data sets used in CDF comparisons of wave elevations, wave crests, and wave heights	19
1.2	Observed statistics of the three (zero-mean) measured wave data sets. Note that these statistics have been estimated from the total durations (see last column of Table 1.1) of the data sets.	19
1.3	Spectral parameters for the four wave data sets	19
1.4	Predicted moments from fitted JONSWAP spectral parameters and from measured spectrum that has been smoothed	20
1.5	Skewness and kurtosis predictions from a consistent second-order analysis vs. exact second-order analysis	20
1.6	Number of simulations and durations (in hours) of each for the four data sets	21
1.7	Means and standard deviations of moments of simulated second-order histories for the four data sets. The standard deviation of the moments reflects the predicted scatter in the durations specified.	23

List of Figures

1.1	Low, Mid, and High frequency components of measured wave history demonstrating presence of phase-locking and potential second-order effects	4
1.2	Skewness and kurtosis comparison for Snorre model test wave measurements and the second-order model	10
1.3	Skewness and kurtosis comparison for Ekofisk ocean wave measurements and the second-order model using fitted H_s , T_p and γ values from measurements	12
1.4	Definition for wave parameters used in the comparison studies	14
1.5	Normalized wave elevation PDF: Data vs. second-order simulations for Set 1 (Snorre wave tank data: Tests 504, 505, 505)	27
1.6	Normalized wave elevation PDF: Data vs. analytical models for Set 1 (Snorre wave tank data: Tests 504, 505, 505)	28
1.7	Normalized wave elevation PDF: Data vs. Hermite models. Elevation from simple Hermite model using predicted moments and cubic Hermite models using predicted and observed moments are shown. . .	29
1.8	Normalized wave elevation CDF: Data vs. second-order simulations and analytical models for Set 1 (Snorre wave tank data: Tests 504, 505, 505)	30
1.9	Normalized wave elevation CDF: Data vs. second-order simulations and analytical models for Set 2 (Snorre data set: Test 304)	31
1.10	Normalized wave elevation CDF: Data vs. second-order simulations and analytical models for Set 3 (Ekofisk data set)	32

1.11	Normalized crest height CDF: Data vs. second-order simulations and analytical models for Set 1 (Snorre wave tank data: Tests 504, 505, 505)	37
1.12	Normalized wave crest CDF: Data vs. Hermite models. Elevation from simple Hermite model using predicted moments and cubic Hermite models using predicted and observed moments are shown.	38
1.13	Normalized wave crest CDF: Data vs. second-order simulations and analytical models for Set 2 (Snorre data set: Test 304)	39
1.14	Normalized wave crest CDF: Data vs. second-order simulations and analytical models for Set 3 (Ekofisk data set)	40
1.15	Normalized wave height CDF: Data vs. Second-order simulations and analytical models for Set 1 (Snorre wave tank data: Tests 504, 505, 505)	43
1.16	Normalized wave height CDF: Data vs. Second-order simulations and analytical models for Set 2 (Snorre data set: Test 304)	44
1.17	Normalized wave height CDF: Data vs. Second-order simulations and analytical models for Set 3 (Ekofisk data set)	45
1.18	Definition for wave parameters used in the comparison studies	48
1.19	Crest height to wave height: Data vs. first- and second-order models	48
1.20	Crest Period T_C to wave period T_W : Data vs. first- and second-order models	49
1.21	Crest front period T_{CF} to crest period T_C : Data vs. first- and second-order models	49
1.22	Wave period T_W to crest height: Data vs. first- and second-order models	50
1.23	Maximum of crest front (T_{CF}) and crest back (T_{CB}) periods to crest height: Data vs. first- and second-order models (for application to "ringing")	50
2.1	Wave spectrum: observed vs. identified first- and second-order	59
2.2	Wave history: observed vs. identified first- and second-order	59
2.3	Identified first-order vs. actual first-order wave history	60
2.4	Wave history in wave tank: observed vs. identified first- and second-order	61

2.5	Wave spectrum in wave tank: observed vs. identified first- and second-order	61
-----	---	----

Chapter 1

Prediction of Second-Order Waves

1.1 Introduction

Nonlinear hydrodynamic effects are of growing interest for ocean structures and vessels. Here we study such effects in one of the most fundamental nonlinearities in ocean engineering: the wave elevation $\eta(t)$ at a fixed spatial location.

It is common practice to model $\eta(t)$ using linear wave theory, which results in a Gaussian model of $\eta(t)$. This ignores the marked asymmetry in the waves: wave crests that systematically exceed the neighboring troughs. Such an asymmetry increases with decreasing water depth. This asymmetry has several practical implications, for example: (1) asymmetric waves are more likely to strike decks on offshore platforms, particularly older Gulf-of-Mexico structures designed with fairly low decks; and (2) unusually large dynamic structural responses have been found in high, steep waves that may not follow linear wave theory.

Second-order random wave models are not new; indeed, they have been a research topic for more than 30 years (e.g., [1, 4, 6, 7, 12, 13, 19, 21, 22, 27]) and remain so today

(e.g., [5, 16, 25, 28]). However, they have not entered common offshore engineering practice, which applies either random linear (Gaussian) waves, or regular waves that fail to preserve $S_\eta(\omega)$, the wave power spectrum. Several drawbacks to second-order random waves may be suggested: (1) they may be inaccurate, for example due to their neglect of higher-order effects; and (2) convenient statistical analysis methods for second-order models are often lacking. We seek to consider both concerns here — the first through comparison of theory with various wave tank and ocean wave measurements. The second issue is addressed by fitting new analytical results for wave moments, and studying the accuracy of using these to construct simple Hermite models of extreme crests.

Note that this study is part of the doctoral studies of the author and this report has largely been adapted from the author's thesis [9].

1.2 Wave Model

Second-order Volterra models [18] have come under increasing use for modeling nonlinear random processes in offshore engineering (e.g. [20, 26, 30]). $\eta(t)$ is accordingly modeled as the sum of a linear (Gaussian) process $\eta_1(t)$ plus a second-order correction $\eta_2(t)$ from the nonlinear hydrodynamic problem associated with waves.

$$\eta(t) = \eta_1(t) + \eta_2(t) \tag{1.1}$$

Before presenting the details of the model, we show the low, mid, and high frequency components of a measured wave tank history in Fig. 1.1 to demonstrate the presence of potential second-order effects in waves. This history is from wave measurements taken during the Snorre Tension-Leg Platform (TLP) model tests [14].

The waves have been measured without the structure in the tank. More details of these wave tank histories are presented in Sec. 1.3. The significant wave height H_s is 14.1m and the spectral peak period T_p is 13.75 seconds. For this example, we chose the mid-frequency component around the spectral peak of the measured history, from 0.025 Hz to 0.14 Hz. The upper bound of 0.14 Hz is chosen to be a little smaller than twice the peak spectral frequency where we expect to see the most dominant second-order wave contribution. The range below 0.025 Hz represents the low-frequency component and the range above 0.14 Hz represents the high-frequency range, in this example. Fig. 1.1 shows that while the low and high frequency components have small energies (standard deviations) as compared to the mid-frequency component, the three components seem to be phase-locked, a phenomenon which would not be seen in a linear process. This observation supports the modeling of the waves as at least a second-order process.

For the second-order $\eta(t)$ in Eqn. 1.1, the standard Fourier sum for the linear part $\eta_1(t)$ is

$$\eta_1(t) = \sum_{k=1}^N A_k \cos(\omega_k t + \theta_k) = \text{Re} \sum_{k=1}^N C_k \exp(i\omega_k t) \quad (1.2)$$

in which Re indicates the real part of a complex number, and $C_k = A_k \exp(i\theta_k)$ are the complex Fourier amplitudes, defined in terms of Rayleigh distributed amplitudes A_k , and uniformly distributed phases θ_k . The C_k 's are mutually independent of one another. The mean-square value of A_k is

$$E[A_k^2] = 2S_\eta(\omega_k)d\omega_k; \quad d\omega_k = \omega_k - \omega_{k-1} \quad (1.3)$$

Based on Volterra theory [18], second-order corrections are induced at the sums

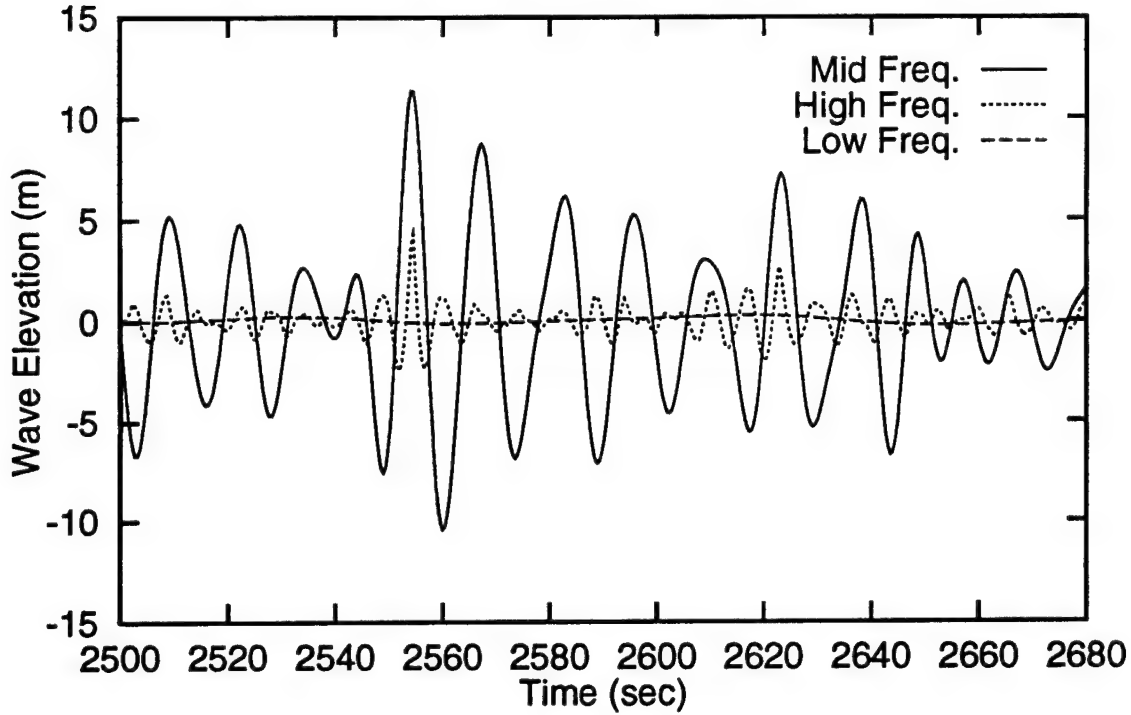


Figure 1.1: Low, Mid, and High frequency components of measured wave history demonstrating presence of phase-locking and potential second-order effects

and differences of all wave frequencies contained in $\eta_1(t)$:

$$\eta_2(t) = \text{Re} \sum_{m=1}^N \sum_{n=1}^N C_m C_n \left[H_{mn}^+ e^{i(\omega_m + \omega_n)t} + H_{mn}^- e^{i(\omega_m - \omega_n)t} \right] \quad (1.4)$$

In general, the functions H_{mn}^+ and H_{mn}^- are known as quadratic transfer functions (QTFs), evaluated at the frequency pair (ω_m, ω_n) . Similar expressions arise in describing second-order diffraction loads of floating structures [10]; in this case the QTFs are calculated numerically from nonlinear diffraction analysis (e.g., [26]).

In predicting motions of floating structures, in view of the relevant natural periods,

interest commonly lies with either H_{mn}^+ (springing) or H_{mn}^- (slow-drift) but not both. For example, in the case of the spar floating structure [10], the slow-drift forces and hence the difference-frequency components generally govern the global motions of the spar. In contrast, in the nonlinear wave problem both sum and difference frequency effects play a potentially significant role. Fortunately, unlike QTF values for wave loads on floating structures, which must be found numerically from diffraction analysis, closed-form expressions are available for both the sum- and difference-frequency QTFs for second-order waves (e.g., [12, 16]). Including the effect of a finite water depth d , for example, the sum-frequency QTF can be written as

$$H_{mn}^+ = \frac{\frac{gk_mk_n}{\omega_m\omega_n} - \frac{1}{2g}(\omega_m^2 + \omega_n^2 + \omega_m\omega_n) + \frac{g}{2} \frac{\omega_mk_n^2 + \omega_mk_n^2}{\omega_m\omega_n(\omega_m + \omega_n)}}{1 - g \frac{k_m + k_n}{(\omega_m + \omega_n)^2} \tanh(k_m + k_n)d} - \frac{gk_mk_n}{2\omega_m\omega_n} + \frac{1}{2g}(\omega_m^2 + \omega_n^2 + \omega_m\omega_n) \quad (1.5)$$

in which the wave numbers k_n are related to the frequencies ω_n by the linear dispersion relation $\omega_n^2 = gk_n \tanh(k_nd)$. The corresponding difference-frequency transfer function, H_{mn}^- , is found by replacing ω_n by $-\omega_n$ and k_n by $-k_n$.

Because $\eta(t)$ is non-Gaussian, interest focuses on its skewness α_3 and kurtosis α_4 . In terms of the significant wave height $H_s = 4\sigma_\eta$, and peak spectral period T_p , these are predicted by a second-order wave model to be of the form:

$$\alpha_3\sigma_\eta^3 = \overline{(\eta_1 + \eta_2)^3} = m_{31}(T_p)H_s^4 + m_{33}(T_p)H_s^6 \quad (1.6)$$

$$(\alpha_4 - 3)\sigma_\eta^4 = \overline{(\eta_1 + \eta_2)^4} = m_{42}(T_p)H_s^6 + m_{44}(T_p)H_s^8 \quad (1.7)$$

The $m_{ij}(T_p)$ are “response moment influence coefficients,” the contribution to response moment (cumulant) i due to terms of order $O(\eta_2^j)$. In general these coefficients are conveniently calculated from Kac-Siegert analysis (Eqns. 12–15, [24, 30]). We assume here the spectrum of $\eta_1(t)$ is of the form $H_s^2 T_p f(\omega T_p)$, so that $\eta_1(t)$ scales in amplitude with H_s and in time with T_p . Such is the form, for example, of a JONSWAP spectrum.

It is useful to define the unitless wave steepness $S_p = H_s/L_p$, in which the characteristic wave length $L_p = gT_p^2/2\pi$ uses the linear dispersion relation. Note that S_p is far less than unity and a second-order perturbation is performed by retaining terms only up to S_p^2 . For deep-water waves the coefficients $m_{ij}(T_p)$ are proportional to L_p^{-j} , and they remain nearly so for finite depths as well. Retaining the leading terms in S_p from Eqns. 1.6–1.7:

$$\alpha_3 = k_3 S_p; \quad \alpha_4 - 3 = k_4 \alpha_3^2 \quad (1.8)$$

In particular, for a JONSWAP wave spectrum with peakedness factor γ , we have fit the following k_3 and k_4 expressions to results for a wide range of depths [28]:

$$k_3 = \frac{\alpha_3}{S_p} = 5.45\gamma^{-0.084} + \left\{ \exp \left[7.41 (d/L_p)^{1.22} \right] - 1 \right\}^{-1} \quad (1.9)$$

$$k_4 = \frac{\alpha_4 - 3}{\alpha_3^2} = 1.41\gamma^{-0.02} \quad (1.10)$$

The second term in this result for α_3 reflects the effect of a finite water depth d : in shallower waters the skewness α_3 grows, as the waves begin to “feel” the bottom. When comparing model predictions to data we will investigate the magnitudes of the omitted (second) terms in Eqns. 1.6, and 1.7.

Note also that while the skewness is predicted to vary linearly with steepness, the

kurtosis is predicted from Eqn. 1.8 to vary quadratically with the steepness S_p . Since the steepness is far less than unity (squared steepness even smaller), this suggests that nonlinear effects will be most strongly displayed by the skewness, and hence by the wave crests rather than the total peak-to-trough wave heights. This second-order model may less accurately predict kurtosis, however, as higher-order omitted effects may be of the same order of magnitude.

In the following sections, we compare predictions from the second-order random wave model to both wave tank data and ocean wave measurements. The comparisons are at the following three levels:

- **Section 1.3: Moments of wave time histories, skewness α_3 and kurtosis α_4 or coefficient of excess $\alpha_4 - 3$.** We will first compare the predicted moments across a broad range of seastates in both the wave tank and the measured ocean data.
- **Section 1.4: Cumulative Distribution Functions (CDF) of wave elevations, wave crests and wave heights.** These comparisons will demonstrate whether or not the second-order model is able to predict the CDFs, over and above predicting the third and fourth moments of the waves.
- **Section 1.5: Local Wave Parameters.** This study investigates the ability of the model to predict local properties of the wave profile; e.g., marginal mean and standard deviation of a wave crest given a wave height, of wave period given a wave height and similar marginal moments of other local wave properties.

1.3 Comparison of α_3 and α_4 : Data vs. Prediction Models

In this section, we shall compare the predicted and observed skewness and kurtosis from two different data sets; one from a wave tank and one from the ocean. The wave tank measurements reflect wave histories with target H_s of 4m to 18m in approximately 308m water depth [14, 15]. We consider 18 wave tank histories each about 2 hours long with a sampling frequency of approximately 0.42 seconds. When estimating moments from the wave tank histories we process hourly portions and as a result have moments from 36 hourly time histories. The ocean wave histories are laser measurements at Ekofisk in the Southern North Sea in approximately 70m water depth. These measurements are for durations of about 18 minutes (2048 samples at time steps of 0.5 seconds) collected every 3 hours during the year 1984. From the annual data set, we select seastates with H_s above 4.5m and with skewness values between -0.05 and 0.4 from the Ekofisk data set. The H_s and skewness cutoffs are introduced to seek to filter out any “noisy” measurements. This resulted in selection of 132 time histories (each of about 18 minutes duration).

Figure 1.2 shows comparisons of predicted skewness and kurtosis with the corresponding sample moments obtained from wave tank histories. Hourly segments of wave tank histories are processed to obtain estimates of skewness and kurtosis, and the predicted skewness and kurtosis are based on Eqns. 1.9 and 1.10. A linear regression (with zero intercept) of observed skewness vs steepness yields an estimated slope of 4.97 ± 0.12 (mean \pm std. error), close to the predicted slope k_3 of 4.93 in Eqn. 1.9 for $\gamma = 3.3$. Note that the target γ values for most of the wave tank tests were 3.3. The

effect of the depth-dependent ($d \approx 308\text{m}$) term in Eqn. 1.9 will cause only a slight increase in the prediction and is neglected here. The seastate-to-seastate scatter σ_{α_3} in the observed skewness values is also consistent; the observed σ_{α_3} is found reasonably well-predicted by that from the simulated hourly segments of second-order seastates (using WAVEMAKER [11]). The simulation is based on a fitted JONSWAP spectrum for each of the hourly measurements. The simulated skewness values show a $\sigma_{\alpha_3} = 0.023$, which is smaller than the observed $\sigma_{\alpha_3} = 0.033$ for the hourly segments of the measurements. The observed seastate-to-seastate kurtosis scatter σ_{α_4} in the hourly measurements is 0.11. In Fig. 1.2b, the mean regression slope of 4.96 ± 0.33 for observed k_4 is about 4 times the predicted k_4 regardless of γ . This lends some support to the view that the second-order model predicts the kurtosis value less accurately due to omitted higher-order effects [25].

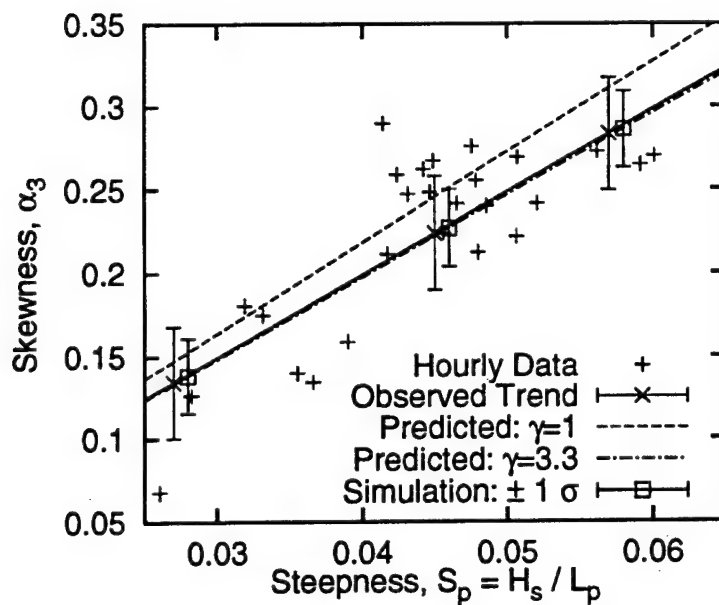
Figure 1.3 similarly compares predicted α_3 and α_4 values to Ekofisk data. For the predicted skewness and kurtosis values, we fit the JONSWAP spectrum parameters to each of observed time histories. $H_s = 4\sigma_\eta$ where σ_η is standard deviation of an observed history. T_p and γ are found from the measured T_z and T_1 , the mean zero-crossing period and the central period, respectively, as shown below. T_z and T_1 are found from measured spectral moments $\lambda_n = \int f^n S(f) df$ as

$$T_z = \sqrt{\lambda_0/\lambda_2}; \quad T_1 = \lambda_0/\lambda_1 \quad (1.11)$$

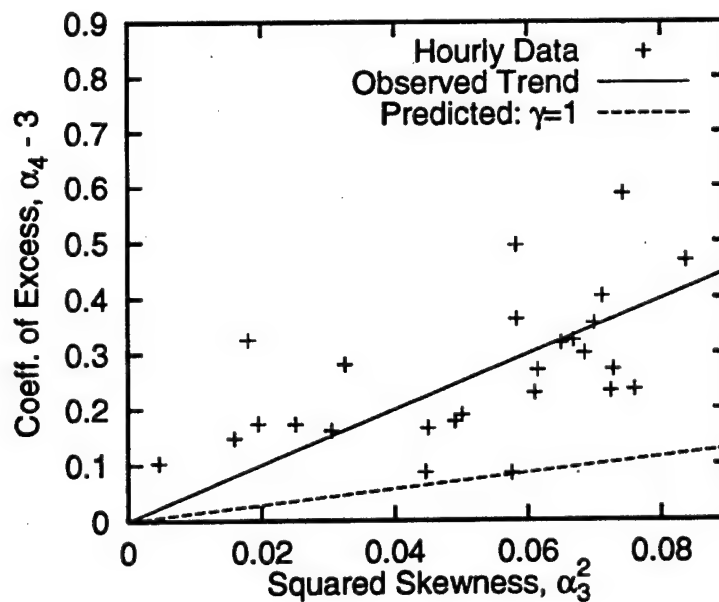
For a JONSWAP spectrum, we have fit these periods and γ for a broad range of bandwidths δ ,

$$\delta = \sqrt{1 - \frac{\lambda_1^2}{\lambda_0\lambda_2}} = \sqrt{1 - \left(\frac{T_z}{T_1}\right)^2} \quad (1.12)$$

A quadratic regression form resulted in the following expressions, for a JONSWAP



(a) Skewness comparison



(b) Kurtosis comparison

Figure 1.2: Skewness and kurtosis comparison for Snorre model test wave measurements and the second-order model

spectrum:

$$\gamma = 458\delta^2 - 423\delta + 96 \quad (1.13)$$

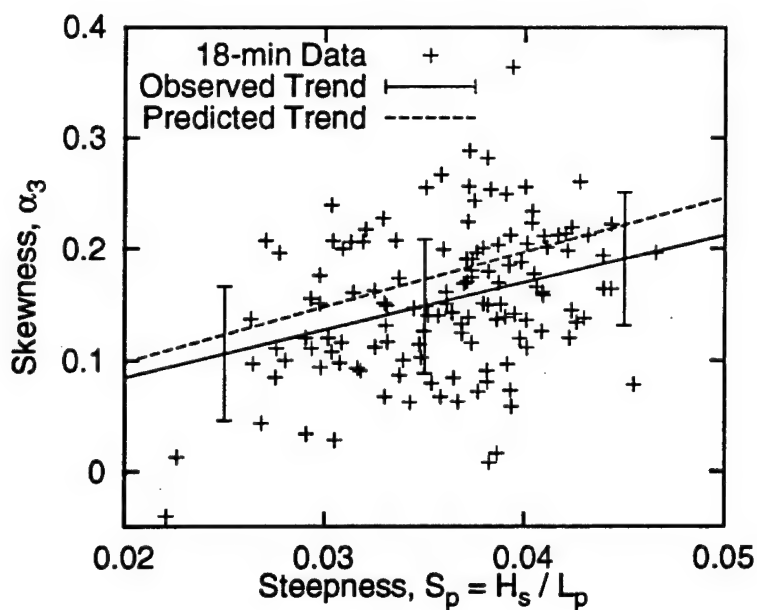
$$T_z/T_p = -0.0023\gamma^2 + 0.0372\gamma + 0.68 \quad (1.14)$$

$$T_1/T_p = -0.0024\gamma^2 + 0.0353\gamma + 0.743 \quad (1.15)$$

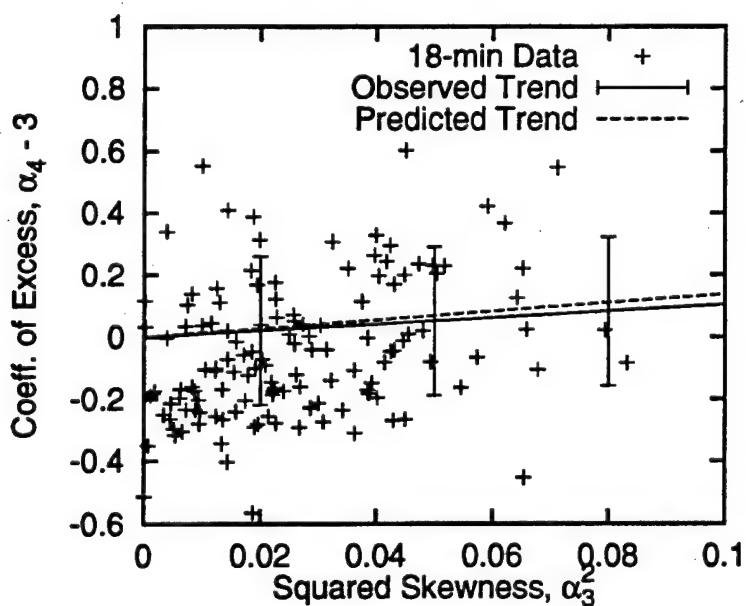
Using the fitted γ (Eqn. 1.13), H_s , T_p (from Eqn. 1.14), we predict skewness and kurtosis using Eqns. 1.9 and 1.10.

For the Ekofisk data set, the slope of the observed trend on α_3 is 4.24 ± 0.14 , while the above prediction scheme indicates a larger skewness trend of 4.92. Note the increase in observed scatter ($\sigma_{\alpha_3} = 0.06$) in skewness compared to the wave tank data. This is due to the noisy estimate of skewness from the 18-minute samples compared to the hourly samples in the wave tank case. The observed trend for kurtosis ($k_4 = 1.03 \pm 0.61$) is also quite accurately predicted by the second-order model (predicted $k_4 = 1.37$), contrary to what we saw for the wave tank data. Again, the kurtosis scatter σ_{α_4} has increased to 0.24 when compared to the hourly estimates for the wave tank data.

The question is: why should the second-order model better match field data than the wave tank data when comparing kurtosis estimates? Recall that the wave tank data represents long-crested waves, while the field data probably represents short-crested sea conditions. The short-crestedness may likely cause a reduction in the nonlinearity in the waves at a point, due to the net effect of waves coming from different directions. In any case, it may seem that the second-order model generally underpredicts nonlinear effects, as seen in comparisons with the wave tank tests. The model prediction, on the other hand, seems better for Ekofisk data set; this may, however, be due to the effect of short-crestedness that leads to reduced nonlinear



(a) Skewness comparison



(b) Kurtosis comparison

Figure 1.3: Skewness and kurtosis comparison for Ekofisk ocean wave measurements and the second-order model using fitted H_s , T_p and γ values from measurements

effects in the measurements.

Owing to the underpredicted kurtosis for wave tank data, it may be anticipated that the second-order model will most likely underpredict the “tails” (extremes) of the distributions for wave elevations, crest heights, and wave heights. On the other hand, for the Ekofisk data set where skewness and kurtosis are well predicted we may hope to find good agreement in predictions and measurements for the wave elevations, wave crests and wave heights. This is studied in detail in the next section.

1.4 Comparison of Distributions of Wave Elevation, Crest Height and Wave Height

In this section, we compare the observed distributions of the wave elevation, crest heights, and wave heights to second-order simulations (using WAVEMAKER [11]). Comparisons of data to analytical or empirical distributions are also presented. A summary of the measured wave data sets follows. Figure 1.4 gives a schematic picture of the definitions of the wave parameters. Crest height is defined as the elevation above mean water level to the highest point between two adjacent mean level upcrossings. Wave height is the elevation difference from the highest to the lowest point between two adjacent mean-upcrossings. The other wave parameters will be discussed in Section 1.5.

1.4.1 Summary of Measured Wave Data Sets

We will compare model predictions to measurements across multiple data sets in order to study the generality of any conclusions made. We focus here on four wave data sets: (1) three 2-hour measurements representing the same seastate from the

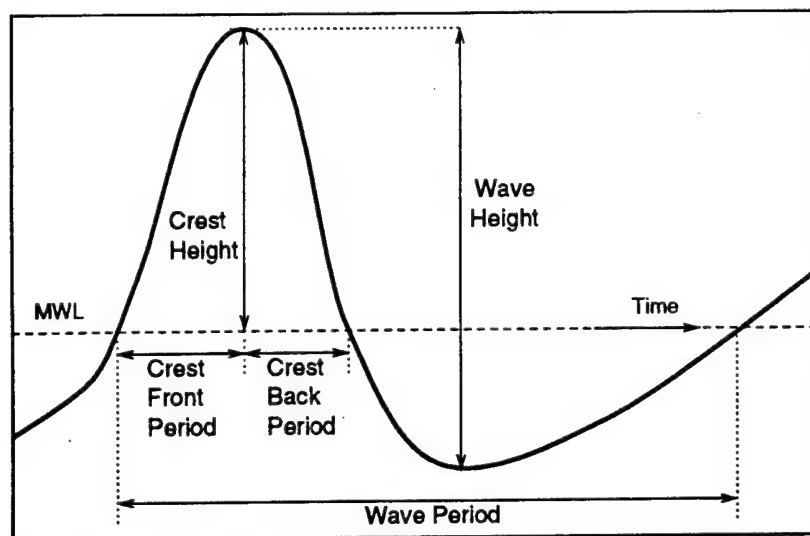


Figure 1.4: Definition for wave parameters used in the comparison studies

Snorre wave tank tests, (2) one 2-hour measurement again from the Snorre wave tank tests, but now representing another seastate, (3) fourteen 18-minute Ekofisk wave measurements representing similar climate conditions. The first data set is chosen because it reflects 6 hours of wave measurement for a severe sea (see Table 1.3). The second data set represents a less severe sea with a different steepness S_p . Out of the year-long Ekofisk measurement, we select time histories that have close H_s and T_p values and, generally, reflect a large S_p value. We present a summary of the three data sets in Table 1.1.

Recall that the first two data sets are wave measurements in the wave tank taken in the absence of any structure. The waves in the wave tank are intended to be long-crested or unidirectional waves. The third data set is for ocean surface measurements taken by a down-looking radar. Since this is a field measurement, we may not expect the waves to be long-crested. The model predictions that follow use only long-crested waves, because no short-crested information is available. The observed wave statistics

for these data sets are summarized in Table 1.2. Here, μ is the mean, σ is the standard deviation, and "Min." and "Max." are the minimum and maximum elevations in the wave histories for the total durations given in Table 1.1.

Of the three sets, the first data set shows the largest nonlinear effects: largest skewness, kurtosis and maximum/ σ values. The last column $\sqrt{2\ln N}$ is an estimate of the most probable Gaussian maximum (or —minimum—) value (normalized by σ) in N cycles. We define the cycle count as $N = T_{\text{dur}}/T_z$ (see Tables 1.1 and 1.3), where T_z is the mean zero-crossing period. In the first data set, note that the normalized maximum (max./ σ) is about 22% larger than the Gaussian extreme, while the normalized minimum value is about 13% smaller than the Gaussian minimum value. This is a manifestation of the nonlinearity (or skewness effect) that makes the crest (maximum) larger and troughs (minimum) smaller. Such nonlinear effects are also seen in the other two data sets, although to a lesser extent. The Ekofisk set, as noted earlier, shows the least nonlinear effects. The seastate steepness S_p also provides a measure of the nonlinearity to be anticipated in the histories, so we will next find the H_s and T_p parameters in order to find S_p .

In order to use the analytic formulations of predicted α_3 and α_4 we fit JONSWAP spectrum parameters (the significant wave height H_s , spectral peak period T_p , and the peakedness factor γ) to the measured spectrum for each of the data sets. In fitting the JONSWAP spectrum to measurements we choose $H_s = 4\sigma$ and we tune T_p and γ so as to best fit the measured spectrum around the peak. The measured spectrum for each data set is found by averaging the spectrum across the different observations in each data set. For example, for the first data set, we average the spectrum of the three tests (504, 505 and 506) to find the final spectrum for this data set. For the second data set, we directly use the measured spectrum, while for the Ekofisk data,

we average across the 14 measured spectra to find the resulting spectrum used in fitting a JONSWAP spectrum.

Table 1.3 shows the target (nominal) and observed JONSWAP spectrum parameters in the wave tank tests. The observed H_s value for Set 1 seems to be different from the nominal H_s values (by about 5%), while observed T_p and γ for Set 1 and 2 seem to agree with the nominal values. For the ocean wave measurements, of course, we do not have any nominal values. A summary of the calculated mean zero-crossing period T_z and the central period T_1 from the measured spectral moments (Eqn. 1.11) is also shown in Table 1.3.

Table 1.4 gives the seastate steepness (based on the fitted H_s and T_p values) along with the predicted moments from Eqns. 1.9 and 1.10. We see excellent agreement in the skewness values for the wave tank data sets, however, as also pointed out earlier on average we underpredict the kurtosis values. Note also that that skewness is overpredicted by about 30% for the Ekofisk data set, when using the fitted skewness form in Eqn. 1.9. This leads to the question of whether accounting for the right spectral shape rather than using the fitted JONSWAP parameters would improve this prediction at all.

To understand the impact of spectral shape on the predicted α_3 and α_4 estimates, we use a smoothed spectrum for each data set and predict the moments using the leading terms in Eqn. 1.6 and 1.7. The averaged spectrum that was used to fit equivalent JONSWAP spectra, contains thousands of frequency components and so a Kac-Seigert analysis that involves an eigenvalue analysis of the frequency components becomes prohibitive. We smooth the averaged spectrum across frequency components, so that the resultant spectrum contains only 256 frequencies. Although this smoothing might lead to some loss in the frequency resolution, we show that

the predicted moments will largely be insensitive to this smoothing. The last two columns (labeled "Smoothed Spectrum") in Table 1.4 are the predicted moments using only the leading terms. A difference in these moments and those from the fitted JONSWAP reflects the impact of spectral shape on the predictions. The kurtosis estimates seem virtually the same across all three sets. For skewness, Set 1 shows about 8% reductions, while Set 3 shows about 5% reduction when using the measured spectrum. When comparing these moments to the measured results, we find that using a smoothed measured spectrum instead of a fitted JONSWAP spectrum does not systematically improve the moment predictions in the three cases.

We investigate next the magnitude of the omitted terms in Eqn. 1.6 and 1.7 for the above moment comparisons for the three data sets. We refer to the second-order prediction as "consistent" when considering only the leading terms in Eqn. 1.6 and 1.7. The predictions where we included all the terms in Eqn. 1.6 and 1.7, is what we refer to as "exact" second-order predictions. Such predictions will describe, for example, the ensemble moments of simulated wave histories from a second-order analysis. These second-order simulated histories contain nonlinearities up to second-order reflected by both the terms in Eqns. 1.6 and 1.7. Table 1.5 compares the moments from a consistent to an exact second-order analysis for the three sets, using the smoothed spectrum in either case. Note that the exact α_3 prediction is smaller than the consistent second-order estimate. This is because the higher-order term in Eqn. 1.6 gives a negative contribution to skewness [16]. The exact analysis gives on average a 10% reduction in skewness from a consistent second-order analysis. The kurtosis values appear to be almost the same in the two analyses, indicating insignificant contributions from the higher-order terms in Eqn. 1.7.

To compare the CDFs of the wave elevations, crest heights, and wave heights we

simulate the first- and second-order wave time histories using WAVEMAKER [11]. The details of the resulting simulations are outlined in the following section.

Table 1.1: Summary information of the four wave data sets used in CDF comparisons of wave elevations, wave crests, and wave heights

Set	Description	Water Depth (m)	Sampling Frequency (sec)	Duration T_{dur} (hours)
1	Snorre wave tank data: Tests 504, 505 and 506	308	0.424264	5.79
2	Snorre wave tank data: Test 304	308	0.424264	1.93
3	Ekofisk data set (Year 1984)	70	0.5	3.98

Table 1.2: Observed statistics of the three (zero-mean) measured wave data sets. Note that these statistics have been estimated from the total durations (see last column of Table 1.1) of the data sets.

Set	σ (m)	α_3	α_4	Min. (m)	Max. (m)	Min./ σ	Max./ σ	$\sqrt{2\ln N}$
1	3.358	0.230	3.263	-11.33	15.90	-3.374	4.735	3.881
2	1.762	0.154	3.141	-6.047	7.944	-3.432	4.509	3.633
3	1.285	0.113	3.012	-5.280	5.490	-4.109	4.272	3.883

Table 1.3: Spectral parameters for the four wave data sets

Set	Nominal Spectrum			Fitted JONSWAP			Calculated	
	H_s (m)	T_p (s)	γ	H_s (m)	T_p (s)	γ	T_z (s)	T_1 (s)
1	14.1	13.75	3.3	13.4	13.75	3.3	11.16	12.
2	7.0	12.0	3.3	7.048	12.0	3.3	9.45	10.05
3	*	*	*	5.14	9.8	3.3	7.62	8.21

Table 1.4: Predicted moments from fitted JONSWAP spectral parameters and from measured spectrum that has been smoothed

	Steepness	Observed		Fitted JONSWAP		Smoothed Spectrum	
Set	S_p	α_3	α_4	α_3	α_4	α_3	α_4
1	0.0454	0.230	3.263	0.224	3.07	0.207	3.06
2	0.0314	0.154	3.141	0.155	3.03	0.153	3.03
3	0.0343	0.113	3.012	0.170	3.04	0.162	3.04

Table 1.5: Skewness and kurtosis predictions from a consistent second-order analysis vs. exact second-order analysis

	Steepness	Consistent 2nd Ord.		Exact 2nd Ord.	
Set	S_p	α_3	α_4	α_3	α_4
1	0.0454	0.207	3.06	0.181	3.07
2	0.0314	0.153	3.03	0.141	3.04
3	0.0343	0.162	3.04	0.143	3.04

Table 1.6: Number of simulations and durations (in hours) of each for the four data sets

Set	No. of Simulations	Duration of 1 simulation	Total duration (hours)
1	20	1.93	38.6
2	10	1.93	19.3
3	50	0.28	14.2

1.4.2 Summary of Simulated Wave Data

The simulations of the first- and second-order histories for the four data sets are based on the measured spectrum of each. The time resolution and the duration of each simulated history are chosen to be the same as those for a single measured history. For example, for the first data set, each simulated history has a duration of 1.93 hours with a time resolution $dt=0.424264$ seconds; similarly, for Set 3 each simulated history contains 2048 points with $dt=0.5$ seconds. A summary of the number of simulations (N_{sim}) and total durations ($N_{sim} \times \text{duration of 1 history}$) of the simulated histories is given in Table 1.6. The number of simulations is generally chosen so that the total simulated durations are longer than the total observed ones. The longer simulations are more likely to “fill in” the tails of the distributions and thereby offer a more robust comparison in the tails.

In order to compare predicted moments to observed results from similar durations, we combine the simulated histories to replicate the total durations in the observed results. For example, in Set 1 we combine (concatenate) 3 histories into 1 and as result have 6 simulated histories each of duration 5.79 hours. Similarly, for Set 3 we combine 14 histories into 1 and as a result have 3 histories each of duration 3.98 hours. For Set 2, we do not need any concatenation since the observed history is itself

1.93 hours long. Of particular interest here, is the scatter in the maximum elevation of simulated histories of different durations.

Table 1.7 summarizes the means and standard deviations of the simulated time histories. These means and standard deviations have been found for moments from the combined histories in each data set. For example, for Set 1 we estimate the moments for the 6 simulated histories each of duration 5.79 hours and then estimate the mean and standard deviations from these 6 values for each moment. Similarly, for Set 3 we find the mean and standard deviations of the moment from 3 simulated histories each of duration 3.98 hours. As Table 1.7 reports, the second-order σ 's are very close to the observed σ 's in Table 1.2 indicating that the second-order corrections contribute insignificantly to the standard deviation of the process.

As noted earlier, the simulated α_3 and α_4 values agree with the predicted moments from an exact second-order analysis in Table 1.5. The largest difference in case of Set 2 is about 9% and this is within the simulated scatter (0.1289 ± 0.0226). These simulated moments, when compared to the observed moments in Table 1.2, appear to be close. The largest discrepancy in α_3 and α_4 is seen in Set 1. We will investigate the impact of these differences between predicted and observed moments on the distributions of elevations, crests, and wave heights in the next section.

1.4.3 Comparison of Wave Elevation Distributions

We first study the comparisons of normalized wave elevation for data set 1, shown in Figure 1.5. The probability density function (PDF) of observed data is shown with $\pm 1 \sigma$ bands on it. This scatter or sigma band of the probability density is estimated as [17]:

$$\text{scatter}, \sigma = \frac{1}{d\eta} \sqrt{\frac{p(1-p)}{N}} \quad (1.16)$$

Table 1.7: Means and standard deviations of moments of simulated second-order histories for the four data sets. The standard deviation of the moments reflects the predicted scatter in the durations specified.

Set	Duration		σ (m)	α_3	α_4	Min. (m)	Max. (m)
1	5.79	Mean	3.3830	0.1815	3.0393	-12.7550	15.0283
		Sigma	0.0411	0.0140	0.0760	0.8195	1.1667
2	1.93	Mean	1.7612	0.1289	2.9855	-6.0894	7.1302
		Sigma	0.0874	0.0226	0.1093	0.8442	0.9656
3	3.98	Mean	1.3060	0.1397	3.0923	-4.9153	6.4073
		Sigma	0.0285	0.0132	0.1412	0.1843	0.5593

where $d\eta$ is the bin-width used, N is the total number of samples in the observation, and p is the estimated probability of being the bin. Note that $1/d\eta$ is included to reflect a probability density scatter. The PDF of the second-order simulation agrees with observed results at almost all probability levels. Note the slight underprediction of elevations around $\pm 3\sigma$ levels. Such a comparison of the PDF plots offers independent comparisons across different elevation levels. The distinctly positively skewed nature of the observed PDF compared to standard Normal PDF $\phi(u)$ in Fig 1.6 shows the non-Gaussianity of the observed elevations. This figure also compares analytical models for elevation distribution to data. Although, the Charlier series (see, e.g., [13]) using predicted moments from fitted JONSWAP spectrum (see Table 1.4) seems to agree here with the observed PDF over the range plotted, the demerits of this series approximation include (e.g., [27]): (1) for extreme elevations the PDF may become negative, and (2) it may show multimodal characteristics not inherent in observations. For example, in Fig. 1.6, the Charlier series shown on log scale could not be plotted below about $-3.5\sigma_\eta$ because the Charlier PDF is negative below this elevation value.

The Hermite model [29] is a cubic transformation of standard Gaussian process based on the first four predicted moments. We present a simplified form of the Hermite

model applicable over a wide probability range for waves. This simplification results because the predicted kurtosis levels for the waves do not significantly affect the transformations, as a result we only need up to the quadratic term in the Hermite transform. At a given fractile, the standard normal variable u can be transformed to a non-Gaussian wave elevation level x in the simplified Hermite model as

$$x = g(u) = \bar{\eta} + \kappa\sigma_{\eta} \left[u + \frac{\alpha_3}{6}(u^2 - 1) \right] ; \quad \kappa = 1/\sqrt{1 + \alpha_3^2/18} \quad (1.17)$$

in which $\bar{\eta}$ is the mean wave elevation. We will compare the predictions of this simplified model to the full cubic-transformation result, which is given as:

$$x = g(u) = \bar{\eta} + \kappa\sigma_{\eta} \left[u + c_3(u^2 - 1) + c_4(u^3 - 2u) \right] ; \quad \kappa = 1/\sqrt{1 + 2c_3^2 + 6c_4^2} \quad (1.18)$$

Optimal values of c_3 and c_4 are found in order to minimize lack-of-fit errors in α_3 and α_4 [29]. Fig. 1.7 compares the Hermite predictions to data, where the three Hermite predictions include:

- simplified model (Eqn. 1.17) with *predicted* moments (labeled "Sim.Herm. w/ Pred.Mom."). Note that this prediction is labeled "Hermite" in Fig. 1.6.
- cubic Hermite (Eqn. 1.18) with *predicted* moments (labeled "Cub.Herm. w/ Pred.Mom.")
- cubic Hermite (Eqn. 1.18) with *observed* moments (labeled "Cub.Herm. w/ Pred.Mom.")

This figure reports virtually no difference in the simple and cubic Hermite predictions using the predicted moments supporting the use of the simple Hermite when using prediction moments from the second-order model. The cubic Hermite model using

observed moments (from Table 1.2) improves the prediction, especially around -3.5σ . Larger extremes have been shown in this figure, to emphasize the elevation difference likely to be seen when using observed or predicted moments in the Hermite predictions. The cubic Hermite model with observed moments appears to best match data; however, this model uses *observed* moments and requires that data be available to find the observed moments. A simplification would be to empirically relate these observed moments to the seastate parameters and use these in the cubic Hermite model. We propose that the simple Hermite model with *predicted* moments from second-order theory offers a convenient alternative to predict a broad range of wave elevations.

Before we look at comparisons of the crest heights (the peaks of the elevation process), we will look again at the wave elevations on a different scale — the CDF or rather the exceedance probability $1-\text{CDF}$. As seen in Fig. 1.8a, the exceedance probability permits comparisons of the cumulative effects of the process. The second-order simulation appears to agree, within the observed scatter, with the observed CDF out to $2\sigma_\eta$. We note a slight underprediction of the observed wave elevation, for example, of about $0.15\sigma_\eta$ at 0.001 exceedance probability. This slight underprediction may have been anticipated in view of the underprediction of the observed kurtosis by the model. A Gaussian model underpredicts the observed wave elevations (see Fig. 1.8b), for example, by about 20% at 0.0001 exceedance probability and the (simplified) Hermite model (Eqn. 1.17) improves the agreement and offers a similar comparison as the second-order simulated result. There appears to be a discrepancy of about 7% (well within the observed scatter shown by error-bars) at the same 0.0001 fractile. As noted earlier, using the observed instead of the predicted moments in the cubic Hermite transformation improves the agreement even in the large extremes.

Both the Hermite models: cubic and simple, however, seem to be within the error-bars of the observed CDF and are considered equally good predictors. Note that in all the figures to follow, the predictions from the simplified Hermite model using the predicted skewness (from Eqn. 1.9) are labeled as "Hermite". A comparison of the second-order simulated crests and the simple Hermite predictions shows that these two seem to agree with each other quite closely at all shown fractiles.

For the second data set, we similarly find the second-order wave elevations to generally agree with the observed results (see Fig. 1.9). The underprediction of observed elevations in the tails seems to be within the observed scatter in the elevations. The Gaussian model systematically underpredicts the elevations (a discrepancy of about 20% at 0.0001 fractile), while the Hermite model improves the agreement (i.e., the discrepancy is now within observed scatter).

Finally, for the third (Ekofisk) data set, the second-order simulation and the Hermite model appear to yield excellent agreement with observed wave elevations (see Fig. 1.10). The Gaussian underprediction also seems to be less severe as compared to the previous two data sets. Recall that this is a field measurement where short-crestedness may cause a reduction in the nonlinear wave effects, so the second-order model, which underpredicts the long-crested waves, seems to better agree with the field data. Further investigations, however, have not been done to verify this hypothesis.

Based on the wave elevation comparisons, we may anticipate the second-order model to best predict the Ekofisk crests, and possibly to slightly underpredict the wave tank crests. We will investigate this in the next section.

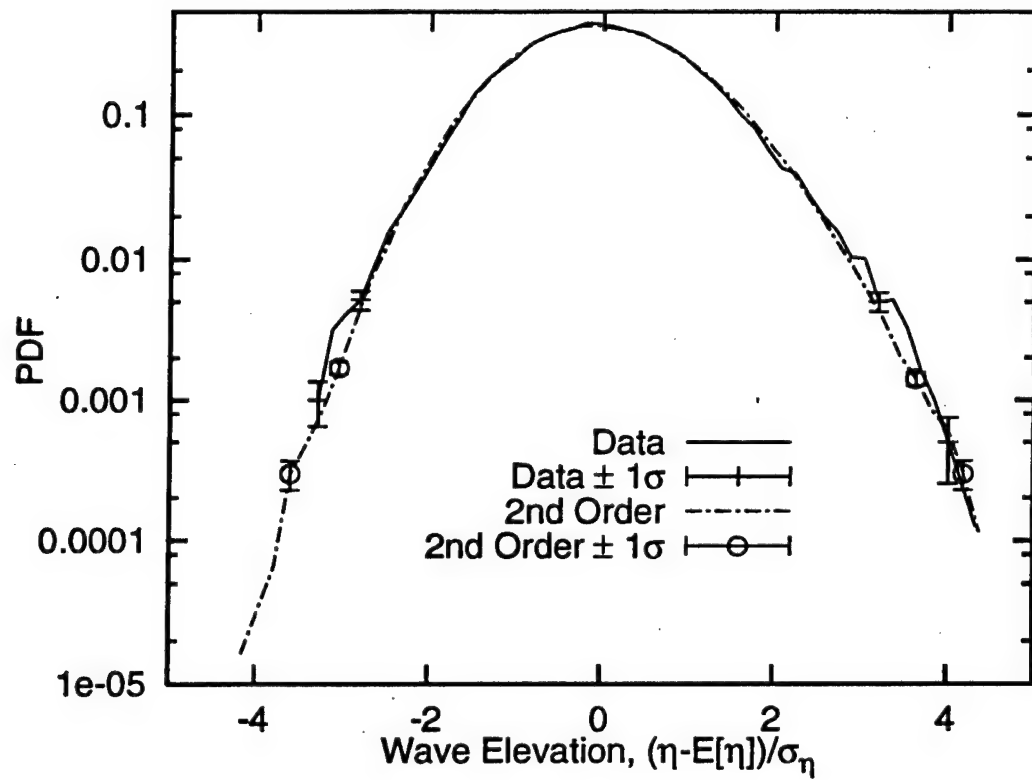


Figure 1.5: Normalized wave elevation PDF: Data vs. second-order simulations for Set 1 (Snorre wave tank data: Tests 504, 505, 505)

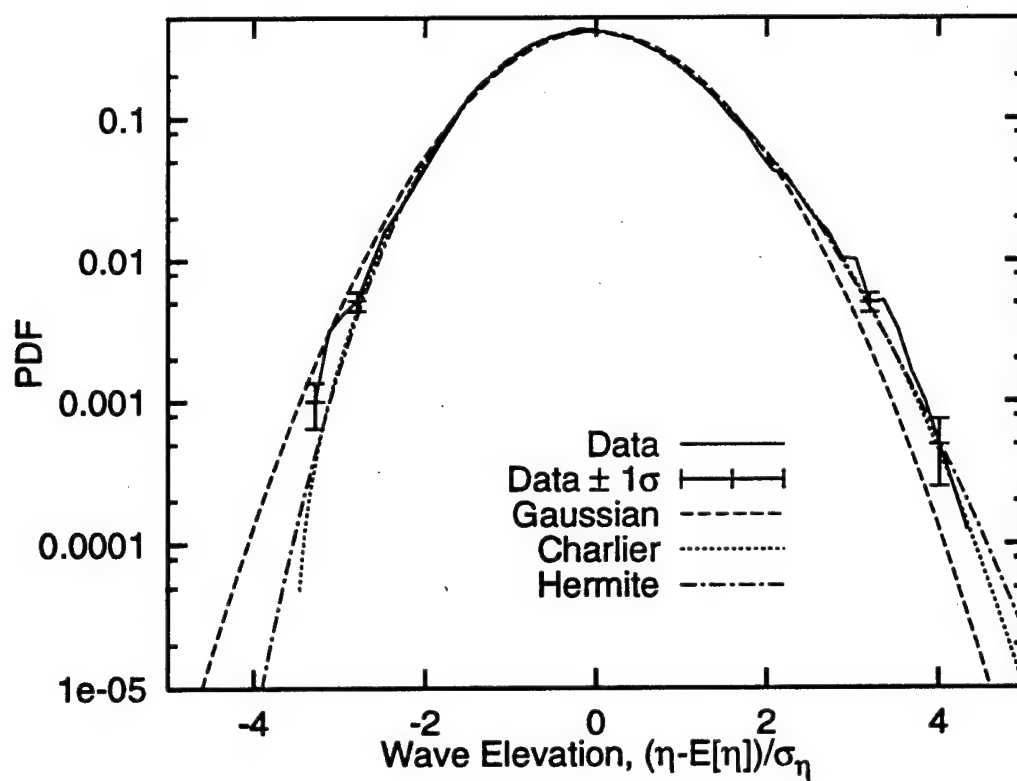


Figure 1.6: Normalized wave elevation PDF: Data vs. analytical models for Set 1 (Snorre wave tank data: Tests 504, 505, 505)

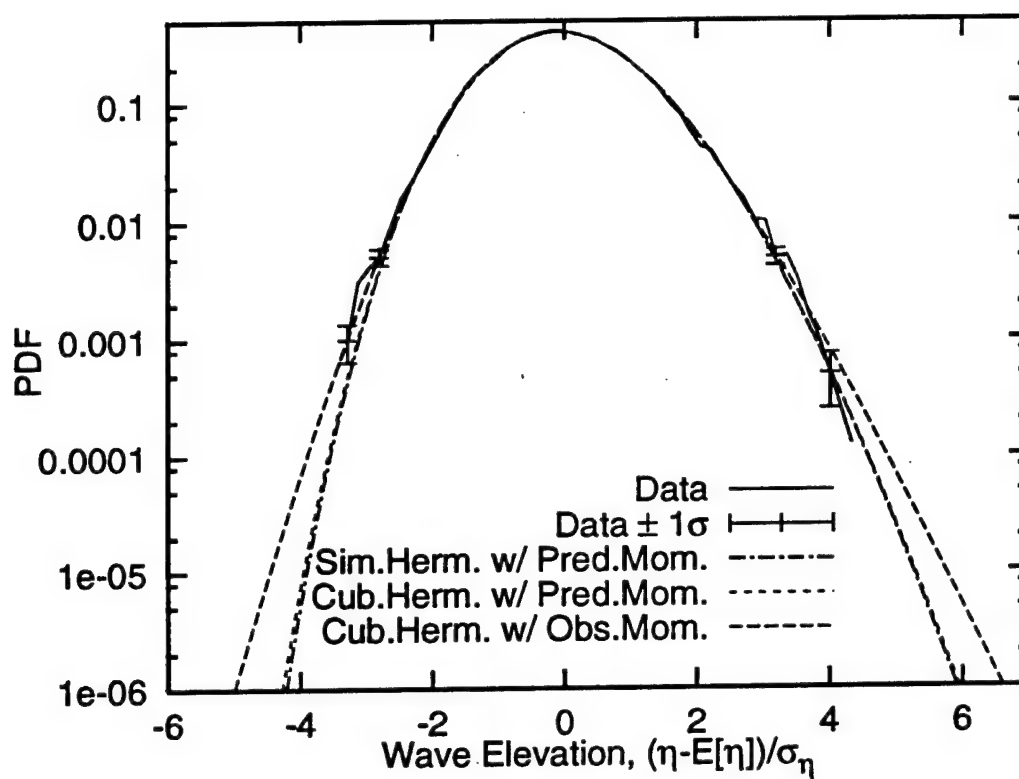
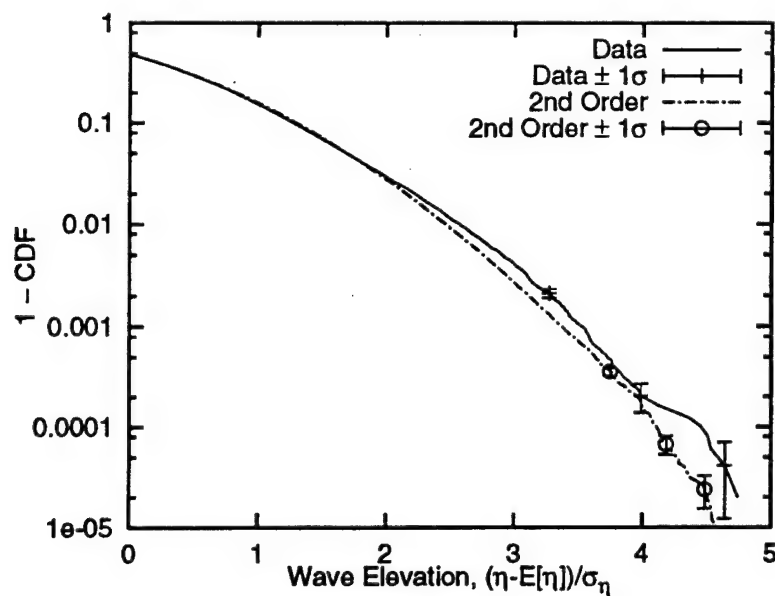
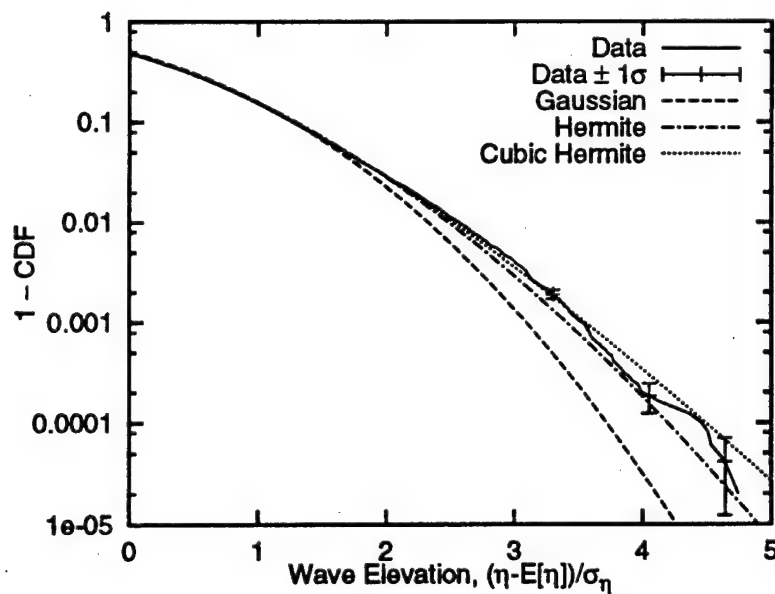


Figure 1.7: Normalized wave elevation PDF: Data vs. Hermite models. Elevation from simple Hermite model using predicted moments and cubic Hermite models using predicted and observed moments are shown.

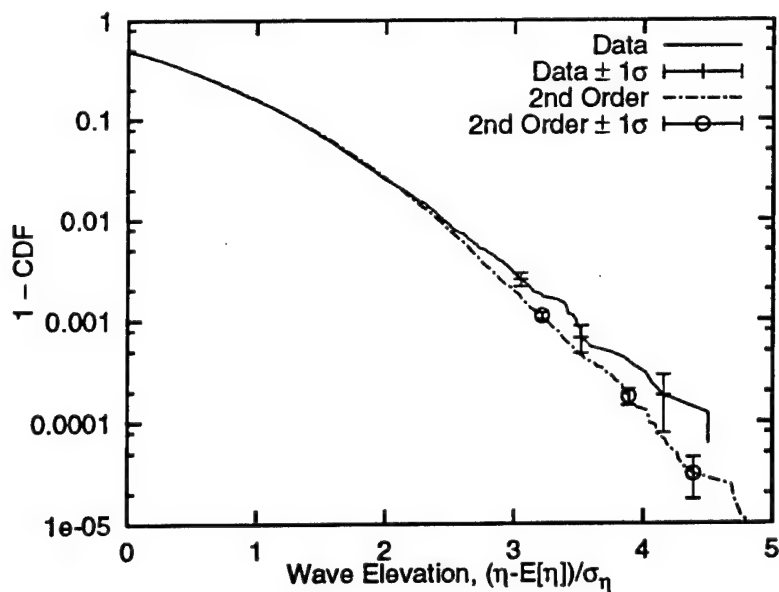


(a) Data vs. Second-order simulation

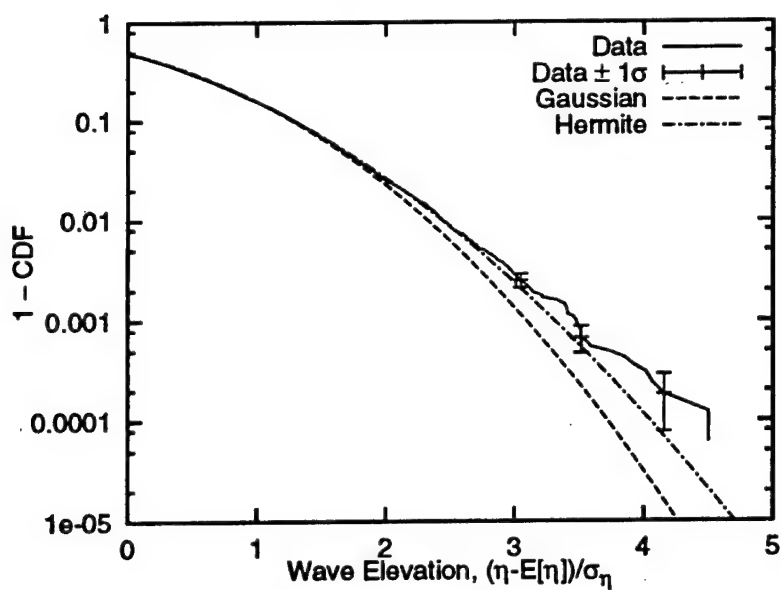


(b) Data vs. Analytical models

Figure 1.8: Normalized wave elevation CDF: Data vs. second-order simulations and analytical models for Set 1 (Snorre wave tank data: Tests 504, 505, 505)

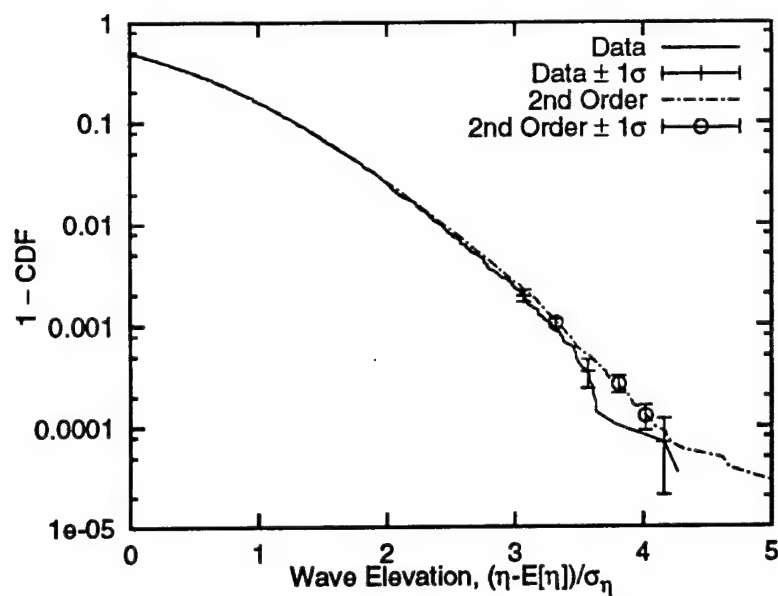


(a) Data vs. Second-order simulation

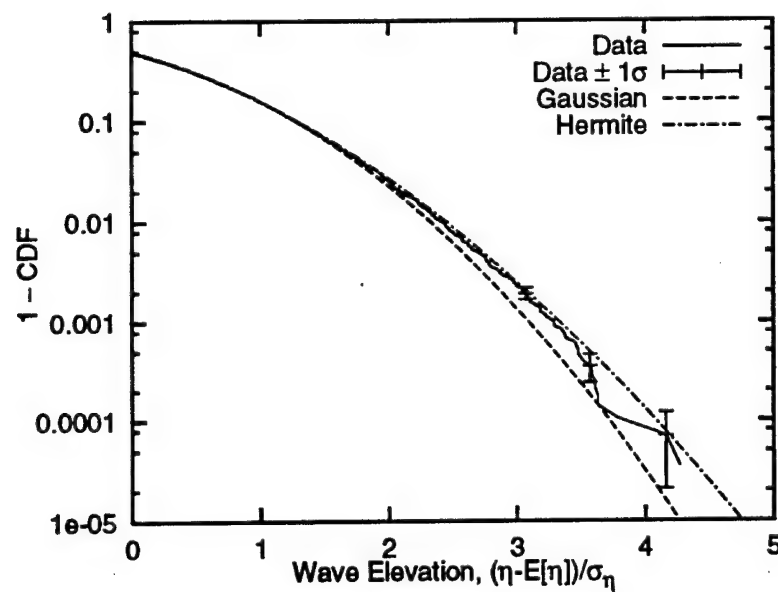


(b) Data vs. Analytical models

Figure 1.9: Normalized wave elevation CDF: Data vs. second-order simulations and analytical models for Set 2 (Snorre data set: Test 304)



(a) Data vs. Second-order simulation



(b) Data vs. Analytical models

Figure 1.10: Normalized wave elevation CDF: Data vs. second-order simulations and analytical models for Set 3 (Ekofisk data set)

1.4.4 Comparison of Crest Height Distributions

The crest height comparison shown in Fig 1.11a for Set 1, shows that while the second-order model accurately predicts the small crests, it appears to underpredict the large observed crests. For example, at 0.001 fractile we find the model underpredicts crests by about 10%. The underprediction in crests heights seems more severe than the wave elevation prediction (see Fig. 1.8). An hypothesis is that the underprediction may be due to higher-order effects. This seems supported at least in the wave elevation case, where the agreement improves when including the observed moments in a cubic Hermite transformation.

Fig 1.11b, which compares the analytical models to data, shows that the Rayleigh crest model given as $\text{Prob}[\text{Crest} > c] = \exp(-0.5(c/\sigma_\eta)^2)$ from linear (Gaussian) wave theory, underpredicts the crests at almost all probability levels of interest (discrepancy of about 25% at the 0.001 fractile). The depth-dependent Haring et al [3] crest height distribution empirically fitted to observed ocean crest data, offers only a slight improvement (discrepancy of about 20% at the 0.001 fractile) over the Rayleigh model. The Haring distribution has been calibrated for a range of water depths less than 200 meters. A similar form was also proposed by Jahns and Wheeler [8]; in this case the wave data comprised of shallow water storm wave records obtained in the Gulf of Mexico. The Haring et al exceedance distribution function is given as

$$\text{Prob}[\text{Crest} > c] = \exp[-0.5(c/\sigma_\eta)^2] \{1 - 4.37(c/d)(0.57 - c/d)\} \quad (1.19)$$

Finally, the Hermite model (a transformation of the Rayleigh crests using Eqn. 1.17) offers a closer fit to observed crests than the Haring distribution. The discrepancy (underprediction) now is about 13% at the same 0.001 fractile level. Note also that

the Hermite prediction agrees well with the second-order simulated crests (compare results across Figs. 1.11a and b).

Fig. 1.12 shows similar results as in Fig. 1.7 where we had investigated the impact of kurtosis on the predicted elevations. We first look at the impact of omitting the predicted kurtosis in the crest prediction. Using analytic predicted skewness and kurtosis (see Table 1.4 for actual values) in the cubic Hermite instead of just skewness in the simple Hermite prediction hardly changes the predicted levels; "Cub.Herm. w/ Pred.Mom." vs. "Sim.Herm. w/ Pred.Mom" are virtually the same in Fig. 1.12. Using the observed moments (see Table 1.2) in the cubic Hermite improves the agreement with observed crests; however, we still see some underprediction in the crest levels around 2 to 3 σ_η . This indicates that even including the correct kurtosis in the cubic Hermite prediction model may not yield perfect crest predictions, implying that other contributing effects may not be predicted exactly. An hypothesis is that, while the Hermite model (using observed moments) predicts the elevations quite accurately, it may still not be modeling the slopes or the velocities of the wave surface and thereby is unable to correctly predict the crests heights. Another hypothesis is that these long-duration wave measurements may be nonstationary. A way of investigating this (not done in this study) may be to divide the measurements into smaller segments and then compare model predictions with observed results from these small segments, where presumably the wave conditions could be assumed to be stationary.

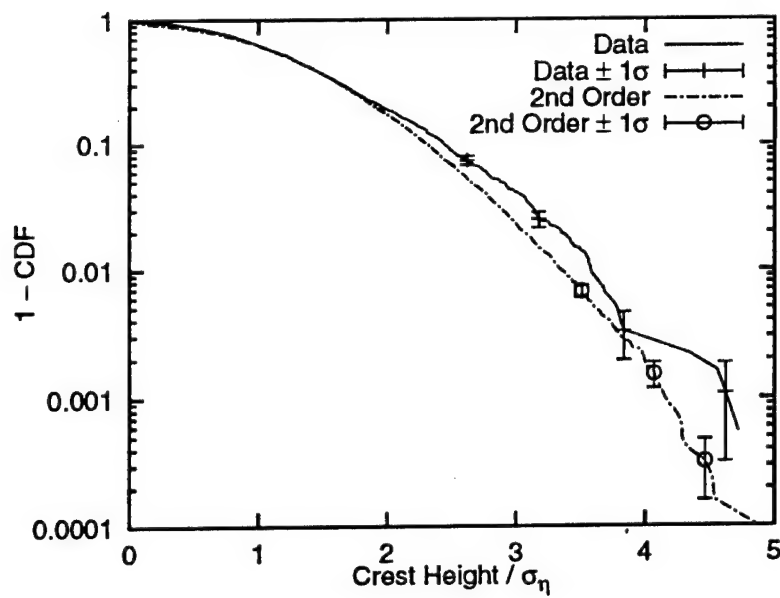
The second data set, again, shows (see Fig. 1.13) similar crest comparisons as in the first set. The second-order simulation offers good agreement for the small crests and underpredicts the large crests (discrepancy of about 12% at 0.01 fractile). Of the analytical models, the Rayleigh distribution underpredicts the observed crests more severely (discrepancy of about 17% at 0.01 fractile). The Haring et al distribution

offers only a slight improvement over the Rayleigh crests, while the Hermite model offers slightly better agreement to observed results (discrepancy of 7% at 0.01 fractile). As anticipated for the Ekofisk data set, the second-order model agrees well with the observed crests (see Fig. 1.14). While the Rayleigh model underpredicts the crests, now both the Hermite and the Haring et al. models seem to agree with the observed crests at all probability levels.

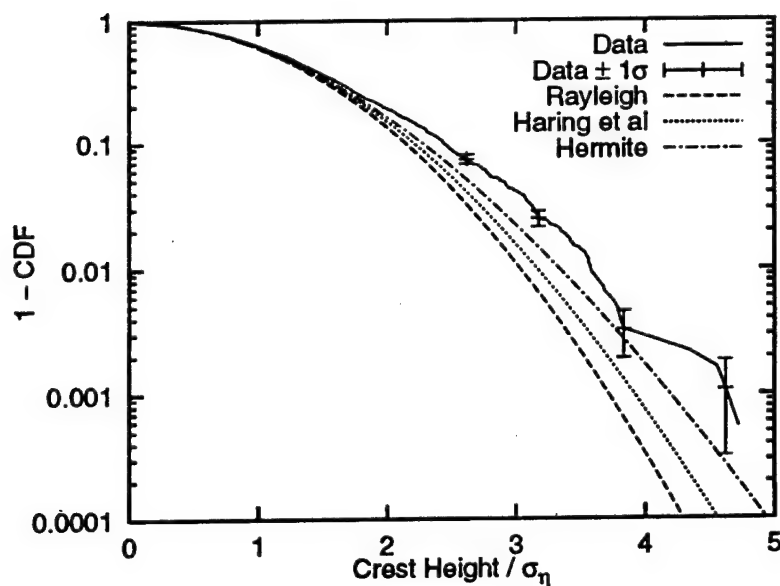
In summary, given that the wave tank data and the field measurements are accurate, we may conclude that while skewness is well-predicted in both types of measurements, the wave tank kurtosis is large than that predicted from a second-order model and the field wave kurtosis can be well-predicted by the second-order model. On the other hand, a hypothesis could be that the wave tank data is in "error" due to its limited ability to generate intended waves. This may be due to scaling issues in the wave tank tests or due to nonstationarity effects in the long measurements. One could on the other hand argue that the field tests may be in error due to measurement noise from the water spray or a direct comparison of field data to the model predictions may be inconsistent due to the presence of short-crested effects in the field data which we are not able to include in the second-order model predictions for lack of information on the directional spread. Recall a third source of error in the field data may be the pooling of the 18-minute histories across different measurements during the year. Further studies along these lines may help explain the differences in the measured results and the model predictions.

We will next look at the model and observed wave heights; we expect any discrepancies to be less severe than seen for the crest comparisons. This expectation is due to the wave elevation being skewness rather than kurtosis-driven; because skewness effects both crests and troughs in compensating ways the wave heights tend, therefore,

to show less nonlinear affects than the wave crests alone.



(a) Data vs. Second-order simulation



(b) Data vs. Analytical models

Figure 1.11: Normalized crest height CDF: Data vs. second-order simulations and analytical models for Set 1 (Snorre wave tank data: Tests 504, 505, 505)

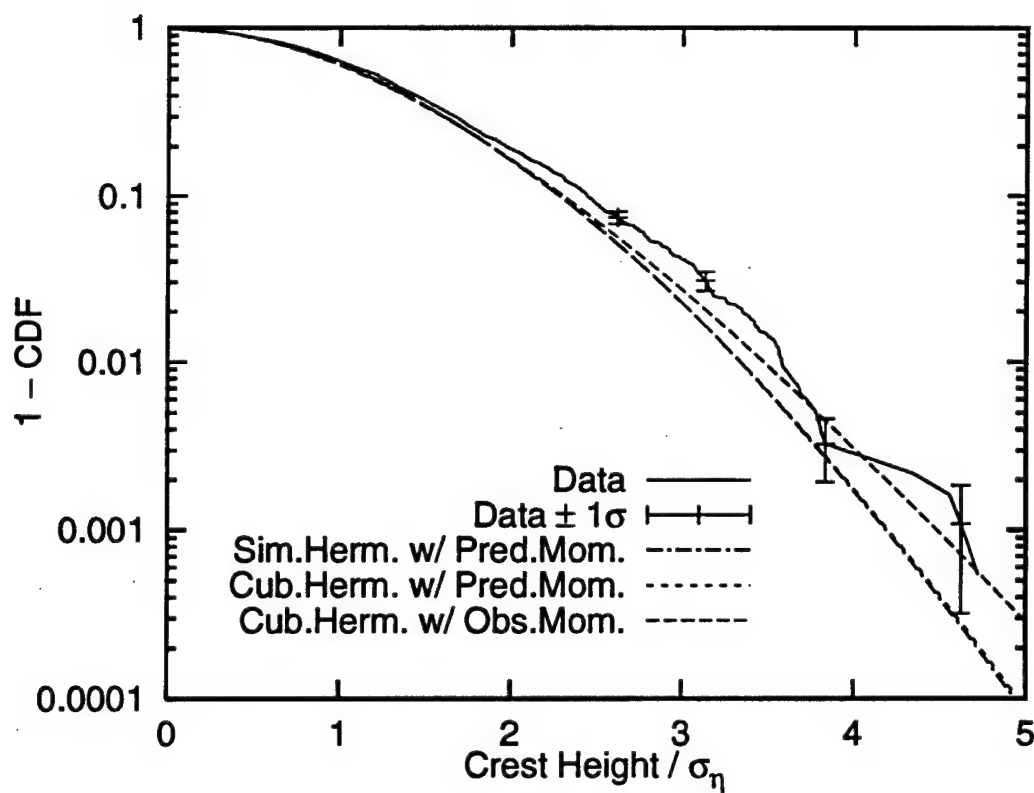
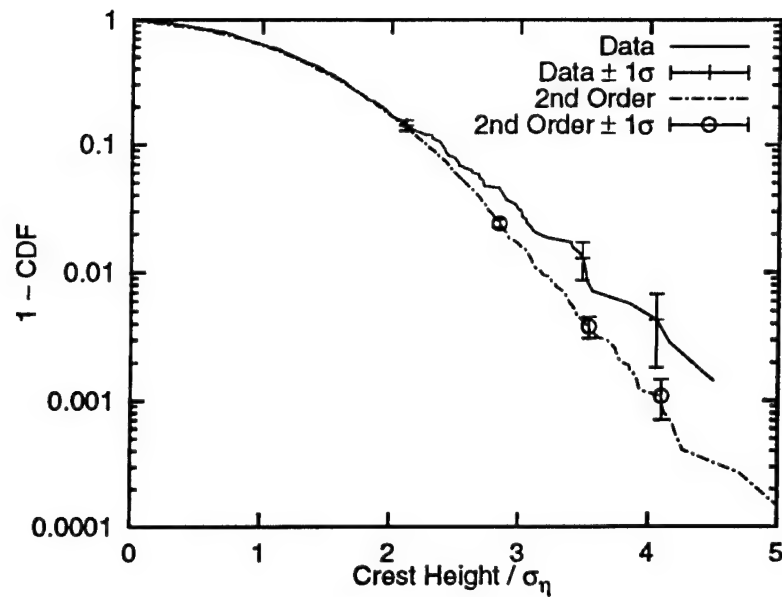
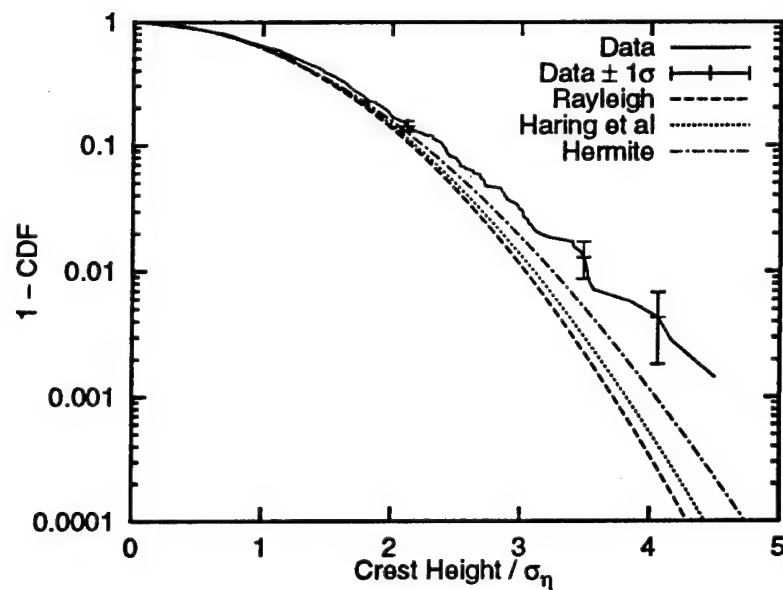


Figure 1.12: Normalized wave crest CDF: Data vs. Hermite models. Elevation from simple Hermite model using predicted moments and cubic Hermite models using predicted and observed moments are shown.

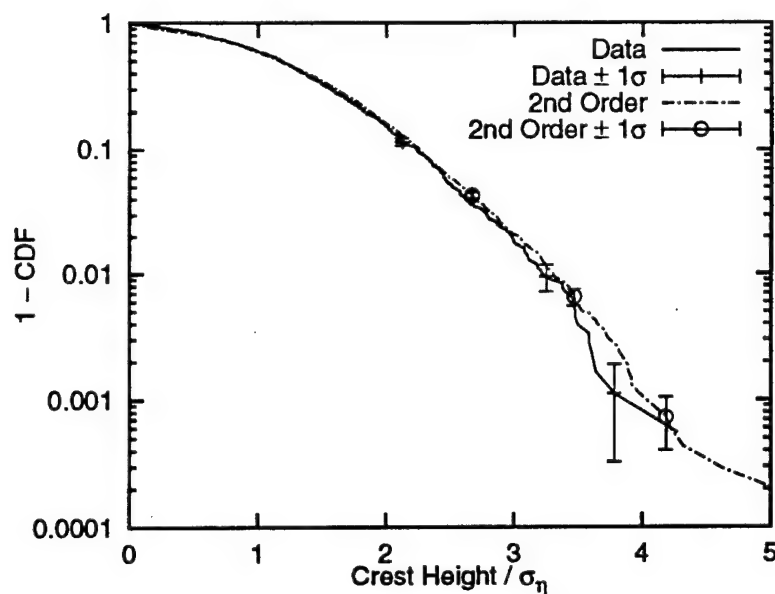


(a) Data vs. Second-order simulation

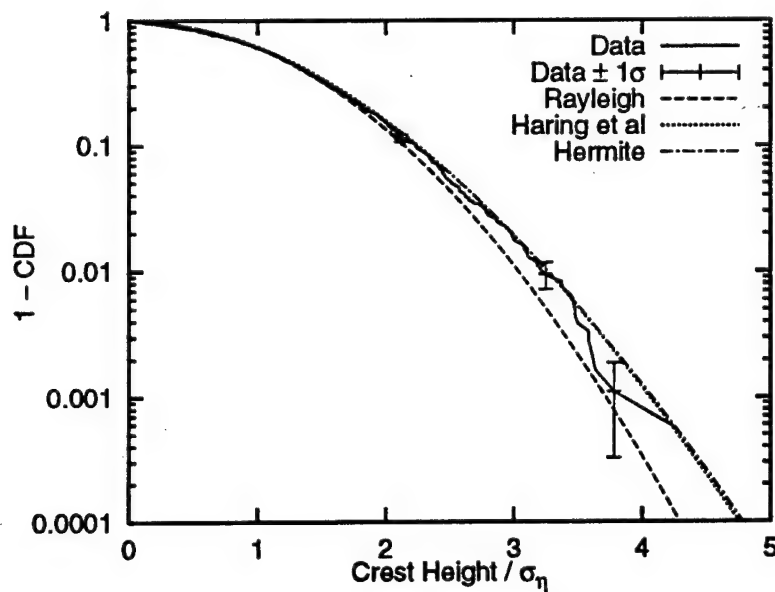


(b) Data vs. Analytical models

Figure 1.13: Normalized wave crest CDF: Data vs. second-order simulations and analytical models for Set 2 (Snorre data set: Test 304)



(a) Data vs. Second-order simulation



(b) Data vs. Analytical models

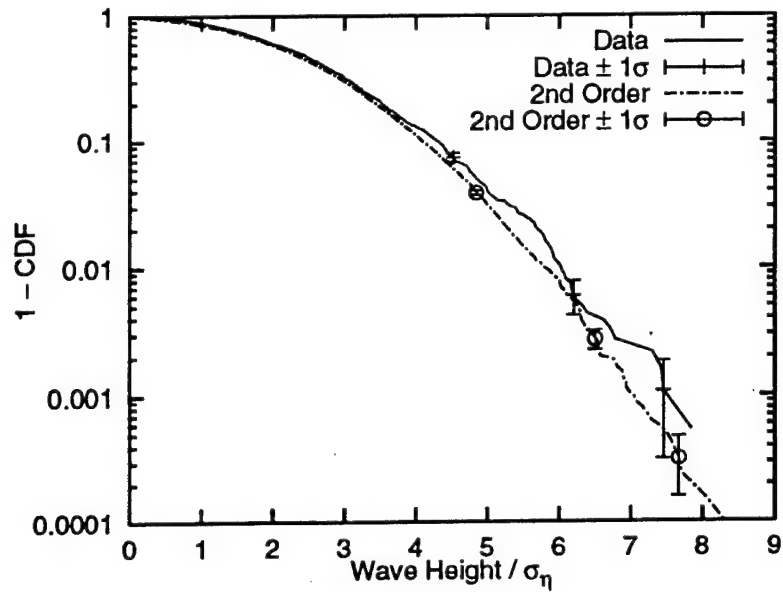
Figure 1.14: Normalized wave crest CDF: Data vs. second-order simulations and analytical models for Set 3 (Ekofisk data set)

1.4.5 Comparison of Wave Height Distributions

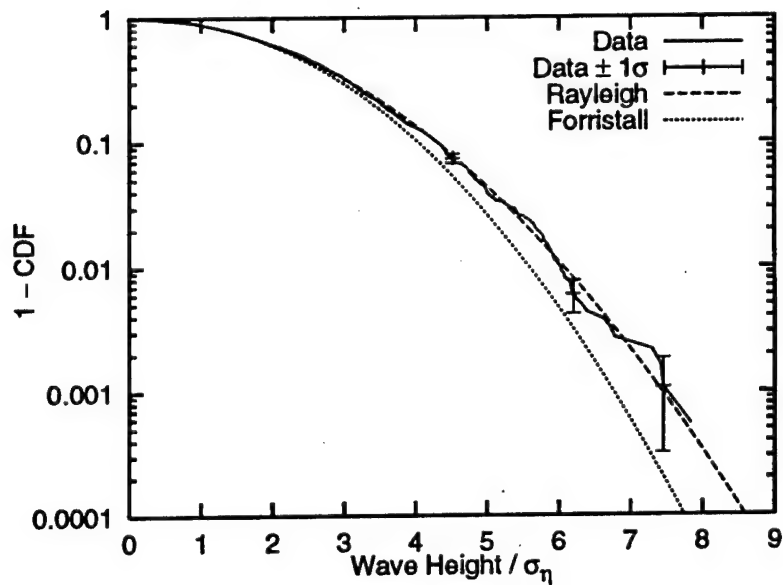
Figure 1.15 compares model and observed wave heights for the first data set. The second-order model offers a closer agreement (within observed scatter) to observed wave heights than the corresponding crest height comparison. For example, at the same 0.001 exceedance probability, the second-order model now underpredicts the observed wave height only by about 6%. Recall the crest height underprediction at this fractile was 10%. Of the analytical models, the Rayleigh model, typically used for wave heights, is given as $\text{Prob}[\text{Height} > h] = \exp[-(h/\sigma_\eta)^2/8]$, while the Forristall distribution [2], an empirical fit to observed ocean wave heights, is given as $\text{Prob}[\text{Height} > h] = \exp[-(h/\sigma_\eta)^{2.126}/8.42]$. The Rayleigh model seems to best fit the observed wave heights, while the Forristall distribution underpredicts the wave heights for this wave tank data. The simplified Hermite wave height prediction, which can now be a transformation of the Rayleigh crests and troughs to make heights, is not shown on the plot. The Hermite model finds the heights by transforming a Rayleigh crest and a Rayleigh trough at a desired fractile using Eqn. 1.17. The transformed crest and trough are added to result in the predicted height at this fractile. Note that in the simplified Hermite transformation the skewness shifts the crest and the trough in the same way so that the wave height remains identical to the Rayleigh height (= Rayleigh crest plus Rayleigh trough). A cubic Hermite transformation that includes the kurtosis effect increases the crest heights and the trough depths depending on the kurtosis magnitude. For kurtosis larger 3, this may only lead to larger wave heights than the Rayleigh distribution. Since the predicted kurtosis values are small, using these in the Hermite model may not significantly affect the wave height results. We choose, therefore, to not show the Hermite wave height model in the comparisons.

A comparison of the wave heights (Fig 1.16) for the second data set offers similar

conclusions as the first data set. The second-order simulation offers good agreement for the small heights and slightly underpredicts the large heights. Of the analytical models, the Rayleigh distribution agrees well with observed wave heights. Finally, the second-order model and observed wave heights agree well for the Ekofisk data set (see Fig. 1.17). Now, however, the Rayleigh model slightly overpredicts the observed heights, and the Forristall distribution agrees well with the Ekofisk heights.

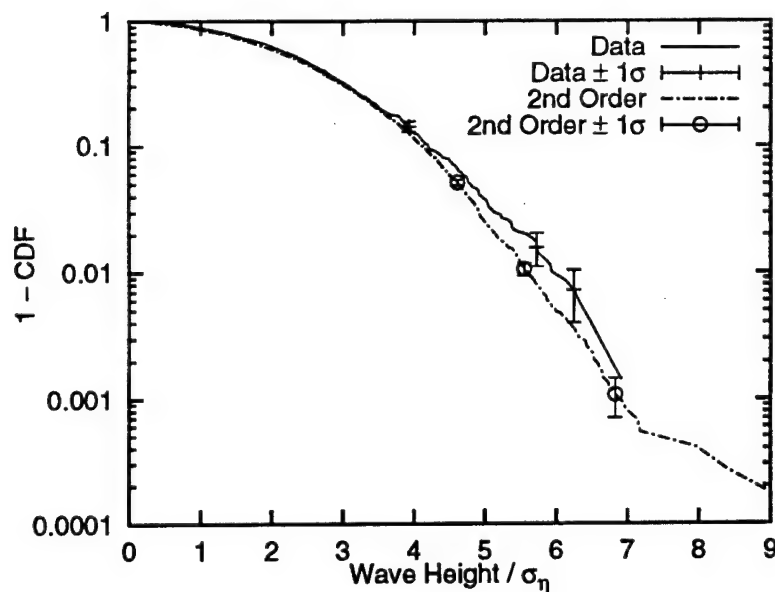


(a) Data vs. Second-order simulation

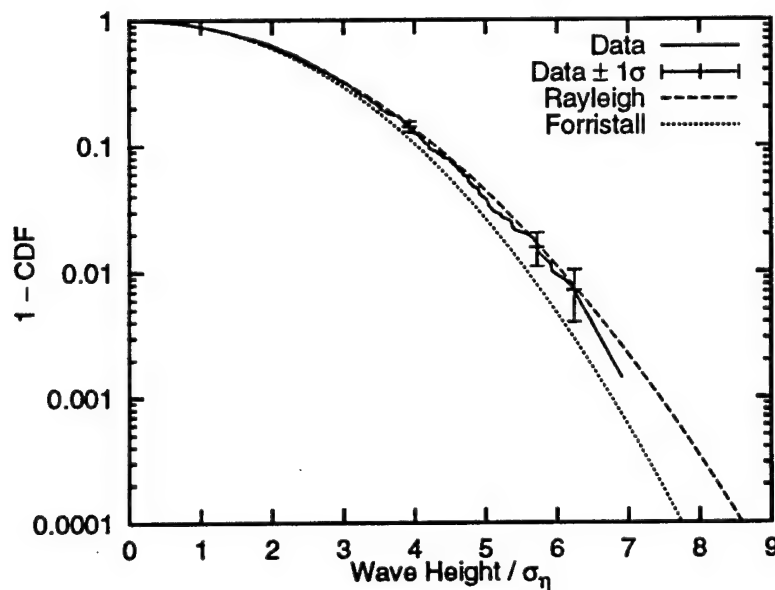


(b) Data vs. Analytical models

Figure 1.15: Normalized wave height CDF: Data vs. Second-order simulations and analytical models for Set 1 (Snorre wave tank data: Tests 504, 505, 505)

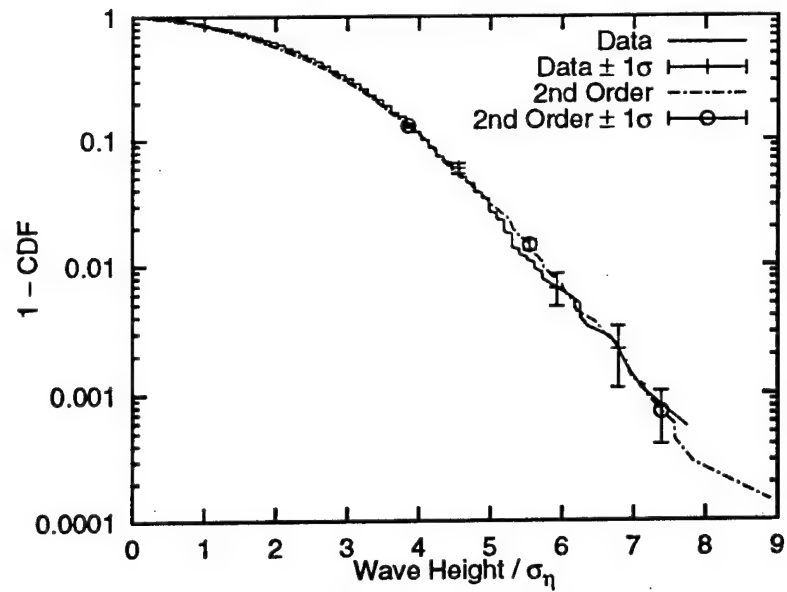


(a) Data vs. Second-order simulation

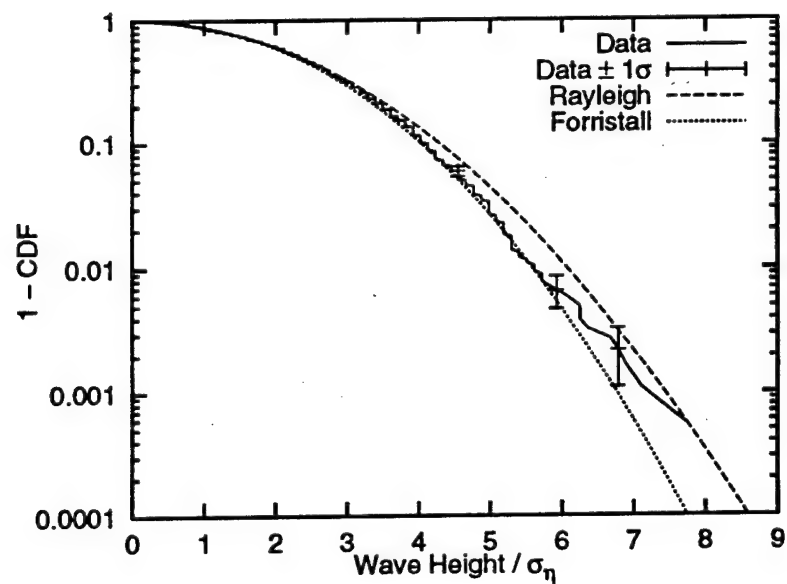


(b) Data vs. Analytical models

Figure 1.16: Normalized wave height CDF: Data vs. Second-order simulations and analytical models for Set 2 (Snorre data set: Test 304)



(a) Data vs. Second-order simulation



(b) Data vs. Analytical models

Figure 1.17: Normalized wave height CDF: Data vs. Second-order simulations and analytical models for Set 3 (Ekofisk data set)

1.5 Comparison of Local Wave Statistics

In this section we compare conditional distributions of local wave parameters. Figure 1.18 defines the local wave parameters to be studied in this section. Crest front period T_{CF} is the period from a mean-upcrossing to the time of occurrence of the highest point in a crest. Crest back period T_{CB} is similarly defined as the period between the highest point in a crest to the following mean-downcrossing. Crest period T_C is the sum of T_{CF} and T_{CB} and is the period between a mean-upcrossing and the following mean-downcrossing in the wave. The wave period T_W , finally, is the period between the two mean-upcrossings in a wave.

We will compare the conditional distribution of the local wave parameters from the second-order model to data. We will demonstrate these comparisons with the first wave data set that represents the Snorre wave tank measurements. We will first look at the conditional distribution of a wave's crest height given its wave height. Figure 1.19 shows the conditional mean and standard deviation of the wave crest given a wave height for the first- and second-order simulated histories and measured data. The Gaussian (first-order) simulation, of course, shows that the crest heights are on average half the corresponding wave heights. The data shows systematically larger crests conditionally, given the corresponding wave height. The second-order model is found to predict this conditional vertical asymmetry quite accurately. Note that even though the model slightly underpredicts the marginal distributions of the crests and of the wave heights, the conditional crest mean and standard deviation seem accurately predicted.

We next consider the horizontal asymmetry in the waves. Figures 1.20 and 1.21 compare T_C to T_W , and T_{CF} to T_C , respectively. As may be expected, the first-order and second-order simulations do not indicate presence of any horizontal asymmetry.

As seen in the figures, T_C is approximately half of T_W . Similarly, T_{CF} is approximately half of T_C . No horizontal asymmetry can be found in the observed data either, indicating that the first- and second-order simulations are statistically equivalent to the observations as regards horizontal asymmetry.

Figure 1.22 shows the conditional distributions of wave periods given crest heights for data, first- and second-order simulations. This figure shows the conditional median along with 16- and 84-percentile spread of wave periods given crest heights. All results show the same trend of increasing wave periods for small to moderate crest heights, and constant wave periods for large crest heights. The asymptotic wave period is close to the central period obtained from the first moment of the wave spectrum (in this case the central period is about 12 seconds, Table 1.3). Figure 1.23 shows a similar comparison of conditional distribution of maximum of T_{CF} and T_{CB} in a wave vs. the crest height of the wave. This is again shown as the conditional median with 16- and 84-percentile scatter of $\text{Max.}(T_{CF}, T_{CB})$ given crest heights. Such statistics are of interest, for example, in identifying the large high-frequency resonant ("ringing") responses that may be observed in offshore structures. Again, all results show the same trend of increasing periods for small crests and a gradual asymptote period for large crest heights, with the second-order model offering a slightly better agreement to data. The asymptotic maximum of the crest front and back period for large crest heights is about 25% of the central wave period.

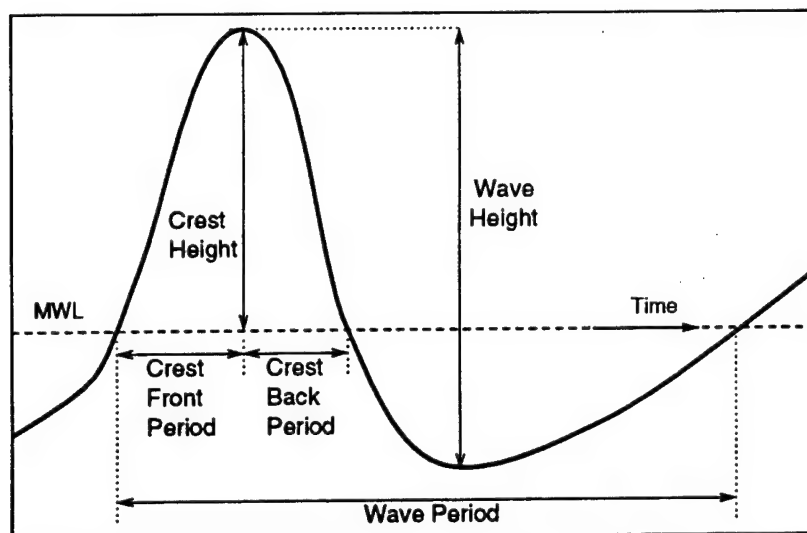


Figure 1.18: Definition for wave parameters used in the comparison studies

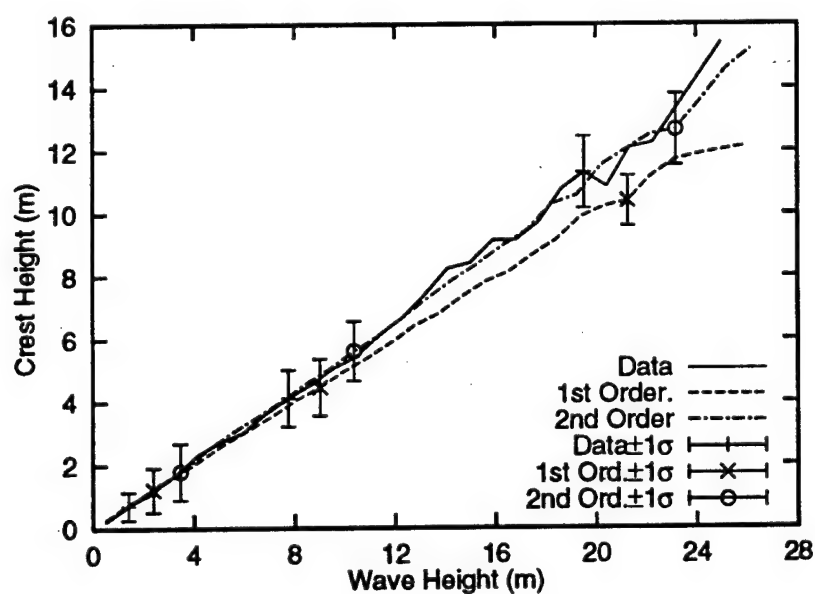


Figure 1.19: Crest height to wave height: Data vs. first- and second-order models

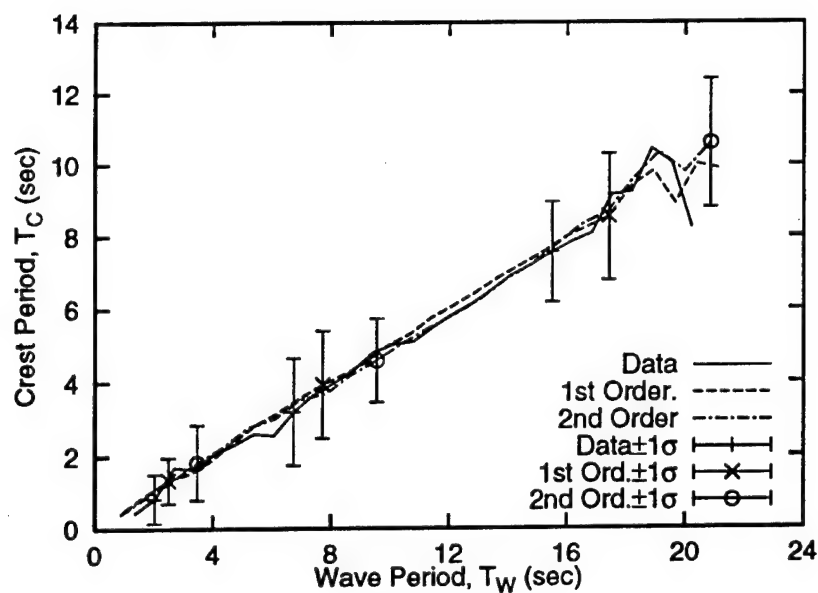


Figure 1.20: Crest Period T_C to wave period T_W : Data vs. first- and second-order models

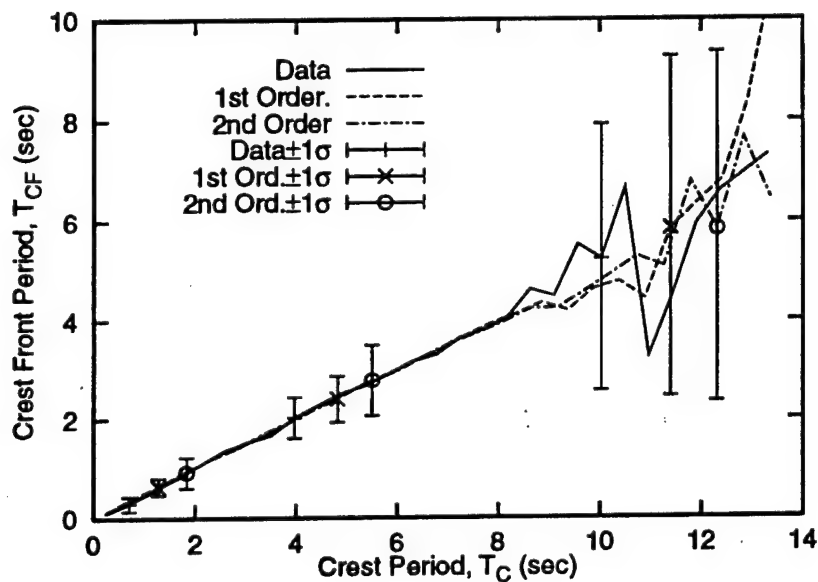


Figure 1.21: Crest front period T_{CF} to crest period T_C : Data vs. first- and second-order models

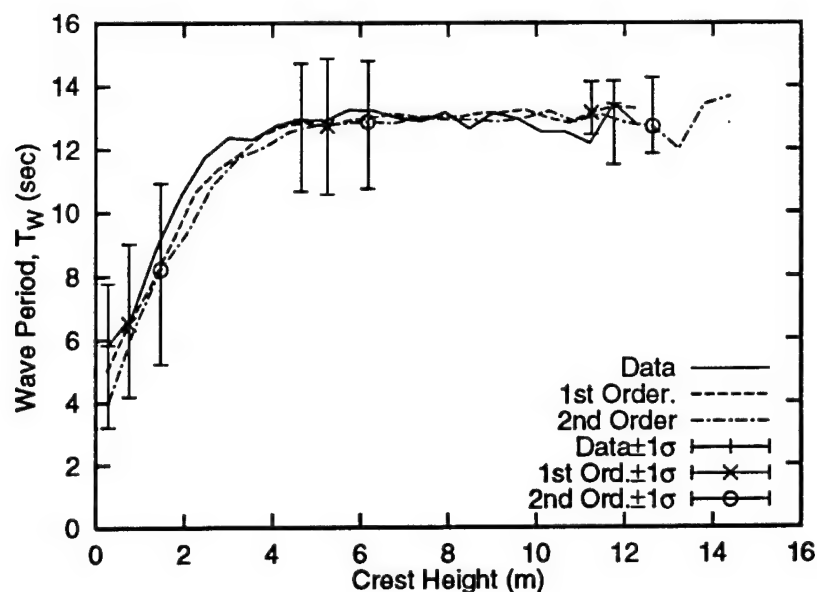


Figure 1.22: Wave period T_W to crest height: Data vs. first- and second-order models

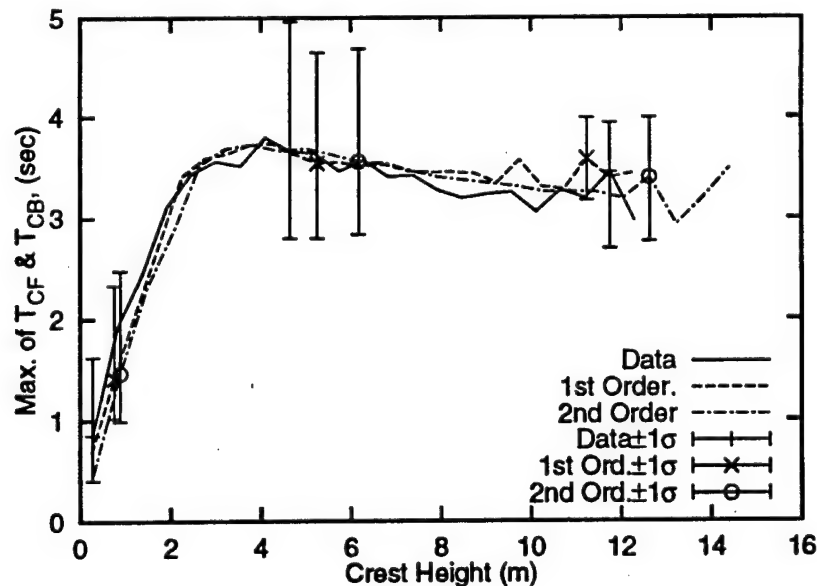


Figure 1.23: Maximum of crest front (T_{CF}) and crest back (T_{CB}) periods to crest height: Data vs. first- and second-order models (for application to "ringing")

Chapter 2

Identification of First-Order Waves

In ocean engineering practice it is common to assume the waves to be Gaussian when estimating forces on large volume structures and any nonlinearity in the waves is embedded in the structural response analysis (e.g., [26]). It has been shown in this chapter that observed time histories generally contain nonlinearities, it is thus imperative to remove any second-order effects in the incident waves so that these effects are not double-counted in the resulting response estimation. Recent studies ([23]) have demonstrated the impact of double-counting such second-order effects on various structural response characteristics. We demonstrate this issue further in the study on the spar floating platform [10].

The methodology to identify the underlying first-order waves is to seek the implied first-order wave history which, when run through the second-order wave predictor, yields an incident wave that agrees with the target observed history at each time point. This identification is performed using a Newton-Raphson scheme to achieve simultaneous convergence at each complex Fourier component. If the observed history has N components, we iteratively solve N simultaneous nonlinear equations to

identify the first-order components. The next section details the methodology of this identification scheme.

2.1 Methodology

The idea here is to identify the implied first-order history $\eta_1(t)$ (of an observed history $\eta_{\text{obs}}(t)$) which, when run through the second-order predictor, yields an incident wave that agrees with $\eta_{\text{obs}}(t)$. The reader is referred to [11] for details on the algorithm.

In the first-order wave process $\eta_1(t)$, see Eqn. 1.2, written as a Fourier sum of N frequencies,

$$\eta_1(t) = \sum_{k=1}^{N/2} A_k \cos(\omega_k t + \theta_k) = \sum_{k=1}^N X_k e^{i\omega_k t} \quad (2.1)$$

we need to identify only the lower half X_k components, since the upper half values are complex conjugates of the lower half. Let us denote $X_k = U_k + iV_k$, where U_k, V_k are the real and imaginary parts of the complex Fourier component X_k , respectively.

The predicted second-order wave process (see Eqn. 1.4) as evaluated from the QTFs is

$$\Delta\eta_2(t) = 2\text{Re} \sum_{m=1}^{N/2} \sum_{n=1}^{N/2} X_m X_n H_{mn}^+ e^{i(\omega_m + \omega_n)t} + X_m X_n^* H_{mn}^- e^{i(\omega_m - \omega_n)t} \quad (2.2)$$

This may be rewritten in the form of a Fourier sum as

$$\Delta\eta_2(t) = \sum_{k=1}^N Y_k e^{i\omega_k t} \quad (2.3)$$

where $Y_k = Y_k^+ + Y_k^-$ are the combined sum and difference frequency components. Here again, Y_k possesses conjugate symmetry so that only the lower half contains

unique information. Y_k^+ can be shown to be

$$\begin{aligned} Y_k^+ &= \sum_{m+n,k} X_m X_n H_{mn}^+ \\ &= \sum_{m+n,k} [(U_m U_n - V_m V_n) + i(V_m U_n + U_m V_n)] H_{mn}^+ \end{aligned} \quad (2.4)$$

where the summation symbol indicates a double summation

$$\sum_{m+n,k} = \sum_{m=1}^{N/2} \sum_{n=1}^{N/2} \text{ such that } \omega_m + \omega_n = \omega_k \quad (2.5)$$

and

$$\begin{aligned} Y_k^- &= \sum_{m-n,k} X_m X_n^* H_{mn}^- \\ &= \sum_{m-n,k} [(U_m U_n + V_m V_n) + i(V_m U_n - U_m V_n)] H_{mn}^- \end{aligned} \quad (2.6)$$

where

$$\sum_{m-n,k} = \sum_{m=1}^{N/2} \sum_{n=1}^{N/2} \text{ such that } |\omega_m - \omega_n| = \omega_k \quad (2.7)$$

The combined predicted wave process is

$$\eta_{\text{pred}}(t) = \eta_1(t) + \Delta\eta_2(t) \quad (2.8)$$

The identification scheme strives to simultaneously match $\eta_{\text{pred}}(t)$ to the observed wave history $\eta_{\text{obs}}(t)$ at every value of t . Alternatively, we can perform the identification in the frequency domain and strive to simultaneously match the predicted Fourier components to the observed Fourier components at all frequencies.

$\eta_{\text{obs}}(t)$ can be represented in the frequency domain as

$$\eta_{\text{obs}}(t) = \sum_{k=1}^N Z_k e^{i\omega_k t} \quad (2.9)$$

where Z_k 's also possess conjugate symmetry. If the first-order components are identified exactly, from Eqn.s 2.1, 2.3 and 2.9 we will have

$$Z_k = X_k + Y_k \quad ; \quad \text{for all } k = 1 \dots N/2 \quad (2.10)$$

Note that the upper half values can be obtained from conjugate symmetry of the lower half values. In the Newton-Raphson identification scheme we will try to simultaneously minimize $X_k + Y_k - Z_k$; for $k = 1 \dots N/2$ to achieve convergence. Now, this scheme requires a Jacobian of $X_k + Y_k - Z_k$ with respect to the unknowns X_k —such a complex differentiation will lead to numerical discontinuities so we will minimize an equivalent real function $\sqrt{\sum_1^N f_k^2/N}$ instead, where for $k = 1 \dots N/2$

$$\begin{aligned} f_k &= \text{Re}(X_k + Y_k - Z_k) \\ f_{k+N/2} &= \text{Im}(X_k + Y_k - Z_k) \end{aligned} \quad (2.11)$$

The identification of the lower half X_k values requires a simultaneous solution of the nonlinear equations in 2.11 such that $f_k \rightarrow 0$ for all $k = 1 \dots N$, or alternately $\sqrt{\sum_1^N f_k^2/N} \rightarrow 0$. We will formulate the Newton-Raphson scheme in vector form as

$$\mathbf{f} = \left[\frac{\text{ReX}}{\text{ImX}} \right] + \left[\frac{\text{ReY}}{\text{ImY}} \right] - \left[\frac{\text{ReZ}}{\text{ImZ}} \right] \quad (2.12)$$

where bold face letters denote vectors, and vectors $\mathbf{X}, \mathbf{Y}, \mathbf{Z}$ contain the complex

Fourier components X_k, Y_k, Z_k , $k = 1 \dots N/2$, respectively. Here, $\left[\frac{\text{Re}X}{\text{Im}X} \right]$ is a vector containing the real part of X in the upper half and the imaginary part of X in the lower half.

Let us denote

$$\begin{aligned} \mathbf{A} &= \begin{bmatrix} \frac{\text{Re}X}{\text{Im}X} \end{bmatrix} = \begin{bmatrix} \mathbf{U} \\ \mathbf{V} \end{bmatrix} \\ \mathbf{B} &= \begin{bmatrix} \frac{\text{Re}Y}{\text{Im}Y} \end{bmatrix} \\ \mathbf{C} &= \begin{bmatrix} \frac{\text{Re}Z}{\text{Im}Z} \end{bmatrix} \end{aligned} \quad (2.13)$$

Note that the vector \mathbf{A} , of length N , is constructed such that lower half values are the real parts of X_k ; $k = 1 \dots N/2$ and the upper half is the imaginary part of X_k ; $k = 1 \dots N/2$. Similarly, \mathbf{B} and \mathbf{C} , each of length N , contain real and imaginary parts of the lower half of the second-order correction and the observed Fourier components, respectively. The elements of \mathbf{A} and \mathbf{B} are denoted by a_l and b_k , respectively, where $l, k = 1 \dots N$. The objective function in vector notation now is

$$\mathbf{f}(\mathbf{A}) = \mathbf{A} + \mathbf{B} - \mathbf{C} \quad (2.14)$$

A first-order Taylor approximation of $\mathbf{f}(\mathbf{A})$ about a given $\mathbf{A}^{(0)}$ is

$$\mathbf{f}(\mathbf{A}) = \mathbf{f}(\mathbf{A}^{(0)}) + [\mathbf{J}] (\mathbf{A} - \mathbf{A}^{(0)}) \quad (2.15)$$

where $[\mathbf{J}]$ is a $N \times N$ Jacobian matrix denoting the derivatives of the elements f_k in vector $\mathbf{f}(\mathbf{A})$ with respect to each of the unknowns a_l in \mathbf{A} where $k, l = 1 \dots N$. The

Newton-Raphson scheme at iteration $p + 1$ is then formulated as

$$\mathbf{A}^{(p+1)} = \mathbf{A}^{(p)} + \mathbf{h} \quad (2.16)$$

where \mathbf{h} , a vector of length N , is found from a Cholesky decomposition followed by a back-substitution scheme from

$$[\mathbf{J}]\mathbf{h} = -\mathbf{f}(\mathbf{A}^{(p)}) \quad (2.17)$$

It can be easily shown from Eqn. 2.14 that the entries $J_{k,l}$ of the matrix $[\mathbf{J}]$ are

$$J_{k,l} = \frac{\partial f_k}{\partial a_l} = \delta_{kl} + \frac{\partial b_k}{\partial a_l} \quad (2.18)$$

where $\partial b_k / \partial a_l$ indicates the partial derivative of b_k with respect to a_l , and

$$\delta_{kl} = \begin{cases} 1 & \text{if } k = l \\ 0 & \text{otherwise} \end{cases} \quad (2.19)$$

To find $\partial b_k / \partial a_l$, recall from notation in 2.13

$$\begin{aligned} b_k &= \text{Re}Y_k & \text{and} & & b_{k+N/2} &= \text{Im}Y_k & \text{for } k &= 1 \dots N/2 \\ a_l &= \text{Im}X_l = U_l & \text{and} & & a_{l+N/2} &= \text{Im}X_l = V_l & \text{for } l &= 1 \dots N/2 \end{aligned}$$

so that from Eqn.s 2.4 and 2.6 we have

$$\frac{\partial \text{Re}Y_k}{\partial U_l} = \sum_{m+n,k} (U_n \delta_{ml} + U_m \delta_{nl}) H_{mn}^+ + \sum_{m-n,k} (U_n \delta_{ml} + U_m \delta_{nl}) H_{mn}^-$$

$$\begin{aligned}
\frac{\partial \text{Re}Y_k}{\partial V_l} &= \sum_{m+n,k} -(V_n \delta_{ml} + V_m \delta_{nl}) H_{mn}^+ + \sum_{m-n,k} (V_n \delta_{ml} + V_m \delta_{nl}) H_{mn}^- \quad (2.20) \\
\frac{\partial \text{Im}Y_k}{\partial U_l} &= \sum_{m+n,k} (V_m \delta_{nl} + V_n \delta_{ml}) H_{mn}^+ + \sum_{m-n,k} (V_m \delta_{nl} - V_n \delta_{ml}) H_{mn}^- \\
\frac{\partial \text{Im}Y_k}{\partial V_l} &= \sum_{m+n,k} (U_n \delta_{ml} + U_m \delta_{nl}) H_{mn}^+ + \sum_{m-n,k} (U_n \delta_{ml} - U_m \delta_{nl}) H_{mn}^-
\end{aligned}$$

Schematically,

$$[J] = [I] + \begin{bmatrix} \frac{\partial \text{Re}Y_k}{\partial U_l} & \frac{\partial \text{Re}Y_k}{\partial V_l} \\ \frac{\partial \text{Im}Y_k}{\partial U_l} & \frac{\partial \text{Im}Y_k}{\partial V_l} \end{bmatrix} \quad (2.21)$$

where $[I]$ is the identity matrix.

2.2 Verification

2.2.1 Identification of components for simulated data

The simulation of second-order waves and the identification of the first-order waves have been implemented in the WAVEMAKER software [11]. We simulated a second-order wave history whose first-order component is characterized by a JONSWAP spectrum with $H_s = 12$ m, $T_p = 14$ s and $\gamma = 3.3$ in 70 m water depth. We used the net second-order simulated history and tried to identify its first-order wave component using the above-mentioned methodology. A successful identification is implied if the identified first-order component matches the input first-order time history time point by time point.

Figure 2.1 shows the wave spectrum of the simulated history and the identified first-order spectrum along with the corresponding second-order wave spectrum. We see that small second-order contribution to the power spectrum, roughly a decade

below the first-order spectrum even at frequencies twice the peak spectral frequency, suggests the difficulty in identifying these components. Figure 2.2 shows the net simulated wave history and the identified first-order wave history in cycles around the maximum crest height. We next compare the identified first-order wave history to the input first-order history for simulation in Fig 2.3. The identified first-order component is almost the same as the underlying (input) first-order component indicating a successful identification of the components of a wave history.

2.2.2 Identification of components for wave tank data

As another example we will identify the underlying first-order wave component for the Snorre wave tank history (Test 504) that reflects a water depth of about 308m. Figure 2.4 shows a portion where the maximum crest height occurs in the measured wave tank history. The figure also shows the identified first-order and the corresponding second-order wave histories. Note how the second-order wave component affects the first-order peaks, amplifying the crests and moderating the troughs. Figure 2.5 shows the wave spectra for the measured history along with the first-order and the second-order spectra. Note that the second-order energy is significantly smaller (even at twice the peak spectral frequencies) than the first-order energy; it is the phase locking of the first- and the second-order components (Fig. 2.4) that leads to larger crests and flatter troughs.

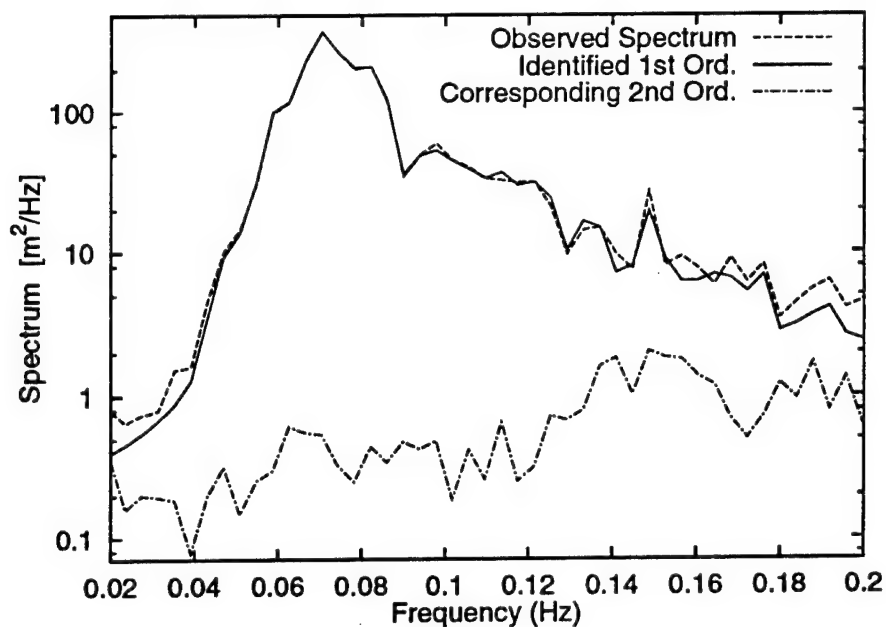


Figure 2.1: Wave spectrum: observed vs. identified first- and second-order

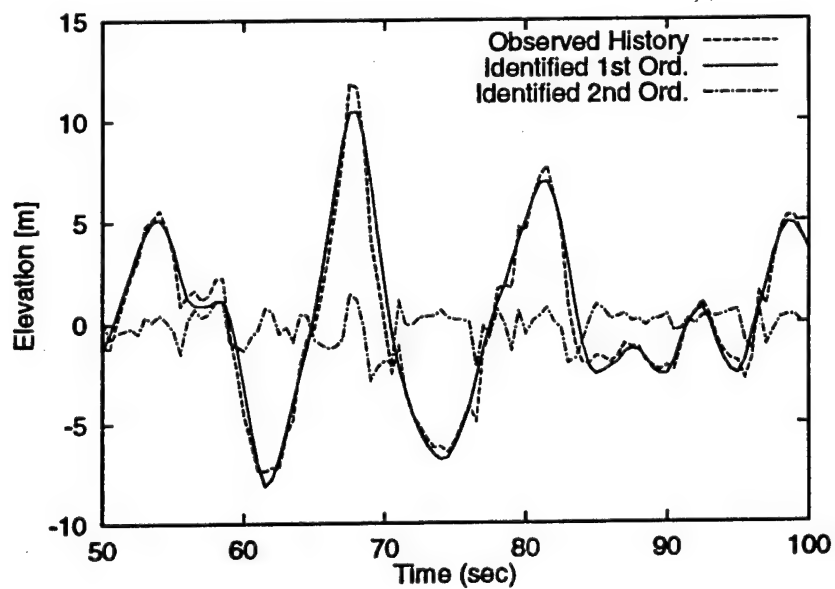


Figure 2.2: Wave history: observed vs. identified first- and second-order

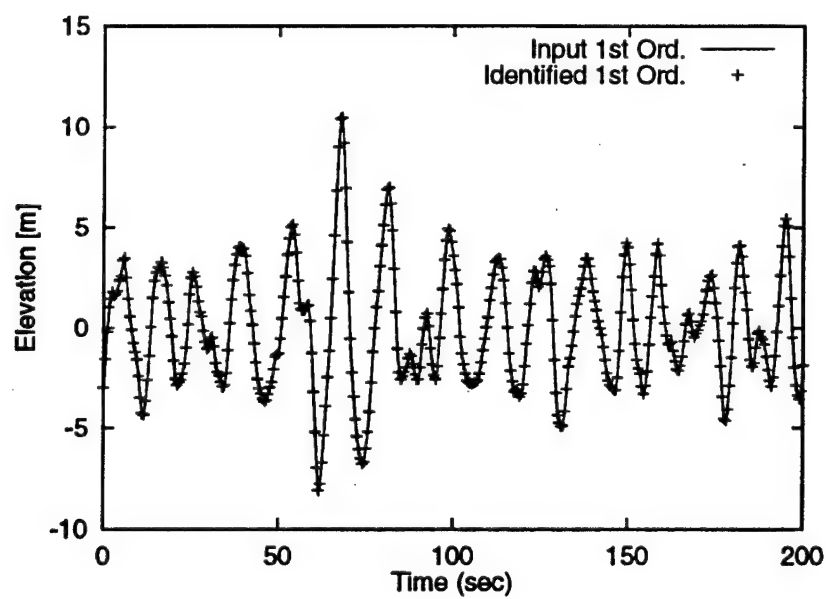


Figure 2.3: Identified first-order vs. actual first-order wave history

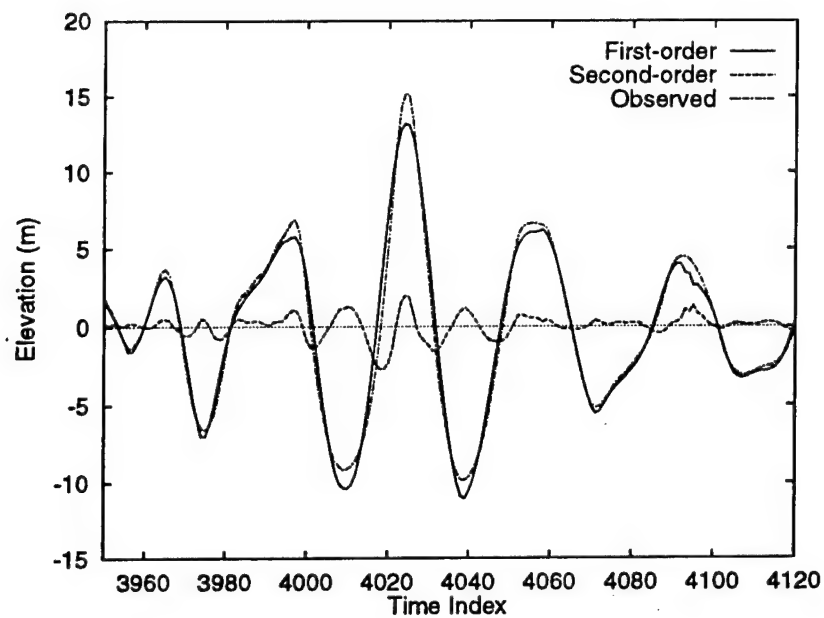


Figure 2.4: Wave history in wave tank: observed vs. identified first- and second-order

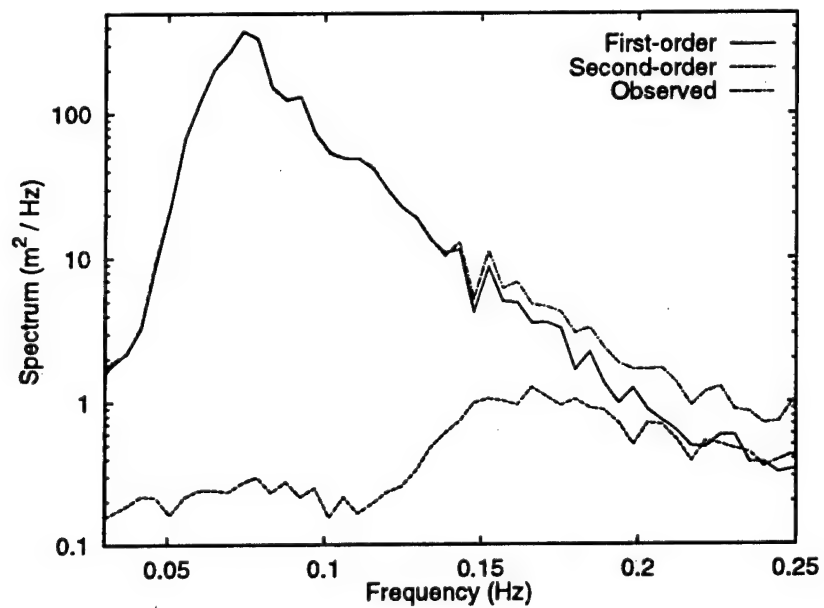


Figure 2.5: Wave spectrum in wave tank: observed vs. identified first- and second-order

Chapter 3

Conclusions and Recommendations

We applied second-order random wave models to investigate the nonlinearities in measured waves (for both wave tank data and ocean field measurements). We found that the second-order model predictions compared well with wave tank results and the agreement was even better in the case of field measurements. We proposed convenient analytic formulations for skewness and kurtosis of waves from second-order theory as a function of the wave environment parameters (H_s , T_p , d) characterizing the climate conditions and the water depth at the site of interest. We also proposed simple analytic crest height distributions based on these predicted moments and found these predicted distributions to compare closely with the measured results. This analytic distributions can also serve as a convenient alternative to simulating second-order wave crests.

We developed a computer program to simulate second-order nonlinear waves. Given a measured time history, this program can also identify the underlying first-order wave component which when run through the second-order predictor produces a resultant time history that agrees with the measured history at every time point.

This feature is especially useful in performing second-order response analysis using measured waves where the input waves are assumed to be Gaussian.

In order to test the limitations of the second-order model, we suggest comparison of model predictions across more severe climate conditions. We found that while the field results were well-predicted, the wave tank crest heights seemed to be underpredicted by the second-order wave model. A more detailed investigation of the wave tank data may help explain these results. Recall that the wave tank data comprised of 2 hour measurements and a hypothesis is that these measurements are long enough to be nonstationary. A way to confirm this hypothesis may be to investigate shorter segments of the 2 hour histories and compare model predictions to measured statistics from these smaller segments. As pointed earlier, scaling down of the waves in the tank may also be a source of error, particularly so when generating waves in severe storms.

For the wave tank data, we found that the prediction of the marginal PDF of the wave elevations was in closer agreement with the measured results than the wave crest predictions. This may suggest that the discrepancy in the wave elevation does not explain the larger discrepancy in the wave crests. A discrepancy, if any, in the comparisons of the upcrossing rates or the velocities of the second-order simulated histories to the measured results may help explain the larger discrepancy in the crest heights.

We found that the cubic Hermite model (using observed moments) slightly underpredicts the crest heights in the two to three σ_η range even though it quite accurately predicts the elevations for the wave tank data. Note that the Rayleigh crests are transformed in this Hermite prediction and consequently assumes an underlying narrow-band process. We could, instead, simulate corresponding Gaussian waves from the measured spectrum in an attempt to reflect the measured bandwidth; and

transform the Gaussian elevations at every time point using the cubic Hermite model with moments of the measured history. A comparison of the crest distribution of this transformed history with the observed crest results will indicate the impact of bandwidth effects on the crest height distribution. Note here that we are attempting to preserve both the observed moments and the observed bandwidths.

Bibliography

- [1] K. Anastasiou, R. G. Tickell, and J. R. Chaplin. The nonlinear properties of random wave kinematics. In *Proceedings of the 3rd International Conference on behavior of offshore structures*. MIT, Massachusetts, 1982.
- [2] G. Z. Forristall. On the statistical distribution of wave heights in a storm. *Journal of Geophysical Research*, 83(C5):2353–2358, 1978.
- [3] R. E. Haring, A. R. Oseborne, and Spencer L.-P. Extreme wave parameters based on continental shelf storm wave records. In *Proceedings of the 15th Coastal Engineering Conference*, pages 151–170, 1976.
- [4] K. Hasselmann. On the non-linear energy transfer in a gravity-wave spectrum. *Journal of Fluid Mechanics*, (12):481–500, 1962.
- [5] S.-L. J. Hu and D. Zhao. Non-Gaussian properties of second-order random waves. *Journal of Engineering Mechanics*, 199(2):344–364, 1993.
- [6] N. E. Huang, S. R. Long, C.-C. Tung, Y. Yuan, and L. F. Bliven. A non-Gaussian statistical model for surface elevation of nonlinear random wave fields. *Journal of Geophysical Research*, 88(C12):7597–7606, 1983.

- [7] R. T. Hudspeth and M.-C. Chen. Digital simulation of nonlinear random waves. *Journal of the Waterway, Port, Coastal and Ocean Division*, 105(WW1):67-85, 1979.
- [8] H.O. Jahns and J.D. Wheeler. Long-term wave probabilities based on hindcasting of severe storms. *Journal of Petroleum Technology*, pages 473-486, April 1973.
- [9] A. K. Jha. *Nonlinear stochastic models for loads and responses of offshore structures and vessels*. PhD thesis, Stanford University, 1997.
- [10] A. K. Jha. Spar floating platform: Numerical analysis and comparison with data. Technical Report RMS-25, Civil Engr. Dept., Stanford University, 1997.
- [11] A. K. Jha and S. R. Winterstein. Simulation and identification of second-order random waves. Technical Report RMS-22, Reliability of Marine Structures Program, Stanford University, Dept. of Civil Engineering, 1996.
- [12] R. S. Langley. A statistical analysis of non-linear random waves. *Ocean Engineering (Pergamon)*, 14(5):389-407, 1987.
- [13] M. S. Longuet-Higgins. The effect of non-linearities on statistical distributions in the theory of sea waves. *Journal of Fluid Mechanics*, 17(3):459-480, 1963.
- [14] MARINTEK. TLP hydrodynamic model tests. Technical Report 511138.01, MARINTEK Trondheim, Norway, 1989.
- [15] MARINTEK. TLP hydrodynamic model tests. Technical Report 511217.01, MARINTEK Trondheim, Norway, 1990.

- [16] T. Marthinsen and S. R. Winterstein. On the skewness of random surface waves. In *Proceedings of the 2nd International Offshore and Polar Engineering Conference, San Francisco*, pages 472–478. ISOPE, 1992.
- [17] A. Papoulis. *Probability, random variables and stochastic processes*. McGraw-Hill, Inc., 1991.
- [18] M. Schetzen. *The Volterra and Wiener Theories of Nonlinear Systems*. John Wiley & Sons, New York, 1980.
- [19] J. N. Sharma and R. G. Dean. *Development and evaluation of a procedure for simulating a random directional second order sea surface and associated wave forces*. PhD thesis, University of Delaware, July 1979.
- [20] SWIM 2.0. *SWIM: Slow Wave-Induced Motions– User’s Manual*. Dept. of Ocean Engineering, M.I.T., 1995.
- [21] M. A. Tayfun. Narrow-band nonlinear sea waves. *Journal of Geophysical Research*, 85(C3):1548–1552, 1980.
- [22] L. J. Tick. A non-linear random model of gravity waves I. *Journal of Mathematics and Mechanics*, 8(5):643–651, 1959.
- [23] T. C. Ude and S. R. Winterstein. Calibration of models for slow drift motions using statistical moments of observed data. In *6th International Offshore and Polar Engineering Conference ISOPE*, 1996.
- [24] T.C. Ude, A.K. Jha, and Winterstein S.R. QTSTAT: Statistics of second-order systems. MAXMIN: Extremes of non-gaussian processes. Technical Report TN-1, Reliability of Marine Structures, 1993.

- [25] T. Vinje and S. Haver. On the non-Gaussian structure of ocean waves. In *Proceedings of the 7th International Conference on the Behaviour of Offshore Structures (BOSS)*, volume 2, pages 453–480, 1994.
- [26] WAMIT 4.0. *WAMIT: A Radiation-Diffraction Panel Program for Wave-Body Interactions—User's Manual*. Dept. of Ocean Engineering, M.I.T., 1995.
- [27] S. R. Winterstein, E. M. Bitner-Gregersen, and K. O. Ronold. Statistical and physical models of nonlinear random waves. In *OMAE - Volume II, Safety and Reliability*, pages 23–31. ASME, 1991.
- [28] S. R. Winterstein and A. K. Jha. Random models of second-order waves and local wave statistics. In *Proceedings of the 10th Engineering Mechanics Speciality Conference*, pages 1171–1174. ASCE, 1995.
- [29] S. R. Winterstein, T. C. Ude, and G. Kleiven. Springing and slow-drift responses: Predicted extremes and fatigue vs. simulation. In *Proceedings of the 7th International Conference on the Behaviour of Offshore Structures (BOSS)*, volume 3, pages 1–15, 1994.
- [30] S. R. Winterstein, T. C. Ude, and T. Marthinsen. Volterra models of ocean structures: Extreme and fatigue reliability. *Journal of Engineering Mechanics, ASCE*, 120(6):1369–1385, 1994.

REPORT DOCUMENTATION PAGE				Form Approved OMB No. 0704-0188		
Public reporting burden for this collection of information is estimated to average 1 hour per response, including the time for reviewing instructions, searching data sources, gathering and maintaining the data needed, and completing and reviewing the collection of information. Send comments regarding this burden estimate or any other aspect of this collection of information, including suggestions for reducing this burden to Washington Headquarters Service, Directorate for Information Operations and Reports, 1215 Jefferson Davis Highway, Suite 1204, Arlington, VA 22202-4302, and to the Office of Management and Budget, Paperwork Reduction Project (0704-0188) Washington, DC 20503.						
PLEASE DO NOT RETURN YOUR FORM TO THE ABOVE ADDRESS.						
1. REPORT DATE (DD-MM-YYYY) <div style="text-align: center;">00-06-1997</div>		2. REPORT DATE <div style="text-align: center;">JUNE, 1997</div>		3. DATES COVERED (From - To)		
4. TITLE AND SUBTITLE <div style="text-align: center;">Nonlinear Random Ocean Waves: Prediction and Comparison With Data.</div>				5a. CONTRACT NUMBER		
				5b. GRANT NUMBER <div style="text-align: center;">N00014-96-1-0641</div>		
				5c. PROGRAM ELEMENT NUMBER		
				5d. PROJECT NUMBER		
6. AUTHOR(S) <div style="text-align: center;">Alok K. Jha</div>				5e. TASK NUMBER		
				5f. WORK UNIT NUMBER		
7. PERFORMING ORGANIZATION NAME(S) AND ADDRESS(ES) RMS Group S. R. Winterstein, C.A. Cornell Blum Center Stanford University, CA 94305				8. PERFORMING ORGANIZATION REPORT NUMBER <div style="text-align: center;">RMS-24</div>		
9. SPONSORING/MONITORING AGENCY NAME(S) AND ADDRESS(ES) OFFICE OF NAVAL RESEARCH 800 N. QUINCY ST. ARLINGTON, VA 22217-4620 ATTN: ROSHDY BARSOUM				10. SPONSOR/MONITOR'S ACRONYM(S)		
				11. SPONSORING/MONITORING AGENCY REPORT NUMBER		
12. DISTRIBUTION AVAILABILITY STATEMENT <div style="text-align: center;">APPROVED FOR PUBLIC RELEASE</div>						
13. SUPPLEMENTARY NOTES						
14. ABSTRACT Convenient analytic formulae are developed to predict the non-linearities in waves and to predict the crest-height distribution in a specified wave environment. These second-order non-linear models are applied to study the properties of random ocean waves. A statistical comparison between the model and measurements is presented. Second-order model predictions are found to agree quite closely with the field measurements, while the wave-tank statistics are under-predicted by the model. Finally, the inverse problem is solved: The underlying first-order wave components are identified and used for second-order prediction. Measured histories are matched point-by-point.						
15. SUBJECT TERMS						
16. SECURITY CLASSIFICATION OF:			17. LIMITATION OF ABSTRACT	18. NUMBER OF PAGES	19a. NAME OF RESPONSIBLE PERSON	
a. REPORT	b. ABSTRACT	c. THIS PAGE			19b. TELEPHONE NUMBER (Include area code)	